

# Primary Macrophage-Based Microrobots: An Effective Tumor Therapy *In Vivo* by Dual-Targeting Function and Near-Infrared-Triggered Drug Release

Van Du Nguyen, Hyun-Ki Min, Ho Yong Kim, Jiwon Han, You Hee Choi, Chang-Sei Kim, Jong-Oh Park,\* and Eunpyo Choi\*

Cite This: *ACS Nano* 2021, 15, 8492–8506

Read Online

ACCESS |

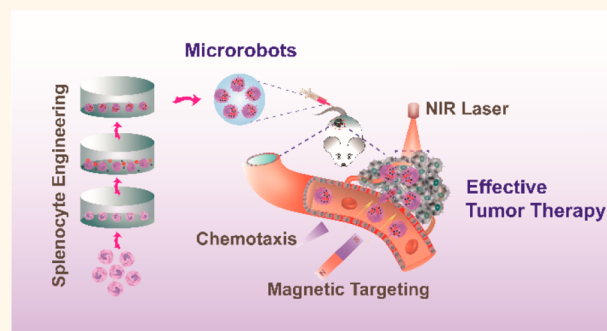
Metrics & More

Article Recommendations

Supporting Information

**ABSTRACT:** Macrophages (MΦs) have the capability to sense chemotactic cues and to home tumors, therefore presenting a great approach to engineer these cells to deliver therapeutic agents to treat diseases. However, current cell-based drug delivery systems usually use commercial cell lines that may elicit an immune response when injected into a host animal. Furthermore, premature off-target drug release also remains an enormous challenge. Here, we isolated and differentiated MΦs from the spleens of BALB/c mice and developed dual-targeting MΦ-based microrobots, regulated by chemotaxis and an external magnetic field, and had a precise spatiotemporal controlled drug release at the tumor sites in response to the NIR laser irradiation. These microrobots were prepared by co-loading citric acid (CA)-coated superparamagnetic nanoparticles (MNPs) and doxorubicin (DOX)-containing thermosensitive nanoliposomes (TSLPs) into the MΦs. CA-MNPs promoted a magnetic targeting function to the microrobots and also permitted photothermal heating in response to the NIR irradiation, triggering drug release from TSLPs. *In vitro* experiments showed that the microrobots effectively infiltrated tumors in 3D breast cancer tumor spheroids, particularly in the presence of the magnetic field, and effectively induced tumor cell death, further enhanced by the NIR laser irradiation. *In vivo* experiments confirmed that the application of the magnetic field and NIR laser could markedly inhibit the growth of tumors with a subtherapeutic dose of DOX and a single injection of the microrobots. In summary, the study proposes a strategy for the effective anticancer treatment using the developed microrobots.

**KEYWORDS:** immune cell, primary macrophage, superparamagnetic nanoparticle, liposome, doxorubicin, synergistic therapy



Over the past few years, the development of micro/nanobiorobots for effective drug delivery applications has attracted great interest from research groups worldwide.<sup>1–3</sup> To construct such biorobots, several research groups have used flagellate bacteria to attach them to the surface of micro/nanostructures containing anticancer/therapeutic agents.<sup>4–7</sup> However, there are limitations associated with the use of bacteria: (1) bacteria are usually harmful and are quickly cleared from the bloodstream by the immune system; (2) the attachment of the bacteria to the micro/nanostructures is challenging and ineffective, limiting the therapeutic potential; and (3) the actuation forces generated by the bacteria are quite small, leading to poor targeting of the microrobots to the target site.<sup>8,9</sup>

Macrophages (MΦs) can offer an alternative and effective method of carrying payloads and therapeutic agents, serving as cellular microrobots.<sup>10–12</sup> These cells are already part of the immune system and, therefore, when administered into the body would not induce an immune response. In addition, they can easily and efficiently engulf (or “phagocytose”) small particles in a process called innate phagocytosis, leading to high therapeutic loading.<sup>13</sup> More importantly, MΦs are

Received: January 5, 2021

Accepted: May 7, 2021

Published: May 11, 2021

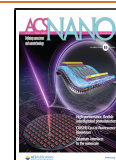
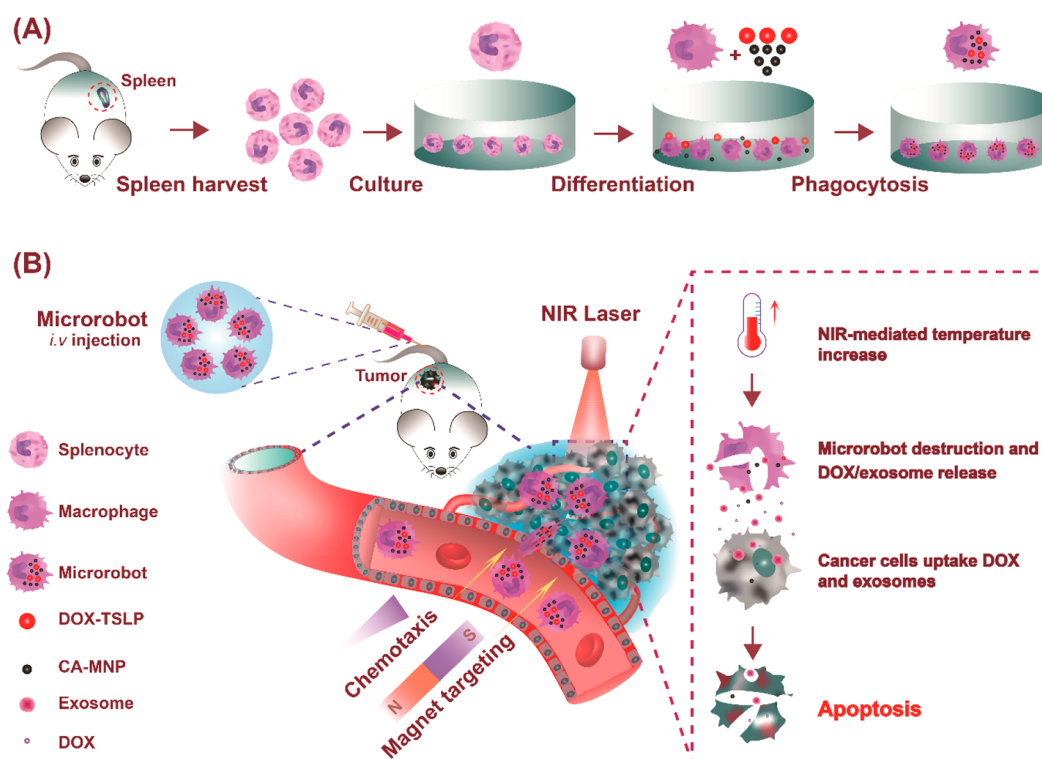


Chart 1. Schematic Representation of the M $\Phi$ -Based Microrobot Working Principles as an Anticancer Therapy<sup>a</sup>

<sup>a</sup>(A) Microrobots are splenocyte-derived M $\Phi$ s loaded with CA-MNPs and DOX-TSLPs. (B) Microrobots are attracted to the tumor site by an electromagnetic field and chemical gradients released by tumor cells. The targeted tumor cells are then destroyed by the NIR-mediated drug release.

circulating cells and can migrate through the blood vessel walls, infiltrate tumors, and stay as tumor-associated M $\Phi$ s, forming up to 70%–80% of tumor mass.<sup>14</sup> Due to this homing ability, these cells could be utilized as potential biocarriers to transport therapeutic agents to tumors. As a result, many macrophage-based drug delivery systems (DDSs) have been developed and appear to have good therapeutic effects. For example, Choi *et al.* utilized monocytes as a “Trojan Horse” delivery system to deliver gold nanoshells to tumor cells and showed excellent therapeutic outcomes after irradiation with the near-infrared (NIR) laser.<sup>14</sup> Similarly, An and co-workers used the RAW264.7 macrophage cell line to deliver small gold nanorods (AuNRs) to breast tumors and then performed tumor hypoxia photoacoustic imaging and photothermal therapy on those tumors.<sup>15</sup> Our group developed a M $\Phi$ -mediated DDS to simultaneously transport AuNRs and liposomes for effectively targeting and treating solid tumors.<sup>16</sup> At the same time, Zhang *et al.* used RAW264.7 cells to deliver doxorubicin (DOX)-loaded silica-based nanocapsules to tumors with promising outcomes.<sup>17</sup> Recently, Huang and colleagues developed a dual function “trojanized” M $\Phi$  to eradicate tumors effectively.<sup>18</sup> However, all of these studies simply used the tumor tropism property of M $\Phi$ s to deliver therapeutic agents to tumors. Therefore, to significantly increase the efficiency of the systems to combat the diseases, such as cancer, additional functions should be incorporated into the cellular systems, to generate microrobots. First, together with their innate chemotactic ability, these microrobots should also be actively controlled to increase the delivery to the targeted areas.<sup>19</sup> Second, they should contain specialized agents responsive to the external

stimulus systems, such as NIR or high-frequency magnetic fields, allowing multimodal treatment of the diseases.

Liposomes are biocompatible and biodegradable nanovesicles that can be loaded with relatively large quantities of hydrophobic or hydrophilic drugs. Some of the liposomal formulations, such as DOXIL, have already been approved for the treatment of tumors. Magnetic nanoparticles (MNPs) have been recently extensively investigated due to their superparamagnetic properties, biocompatibility, and nontoxicity.<sup>20</sup> The inclusion of MNPs into a DDS would allow the application of photothermal therapy, the therapy that generates heat from the light absorption *via* photothermal agents to ablate tumors.<sup>21</sup> MNPs would also “magnetize” the delivery system, allowing the nanoparticles to be actively manipulated through an external magnetic field induced by the electromagnetic actuating system or a permanent magnet.

Here, we developed dual-targeting M $\Phi$ -based microrobots, guided by both the intrinsic tumor homing ability of M $\Phi$ s as well as the external magnetic field to be used as an anticancer therapy (Chart 1). We constructed the microrobots using primary mouse spleen-derived M $\Phi$ s, the cells expected to have a reduced immune response after being engineered, and then injected them back into the mice. We also synthesized and added superparamagnetic nanoparticles coated with citric acid (CA-MNPs) to allow the magnetic field controllability, active targeting, and reactivity to the NIR irradiation. Furthermore, we prepared thermosensitive liposomes (TSLPs) loaded with the anticancer drug DOX for the on-demand drug release from the microrobots. Tumor targeting experiments showed that the microrobots were able to infiltrate the tumor spheroids, and this effect was enhanced by the magnetic field. Our *in vivo*

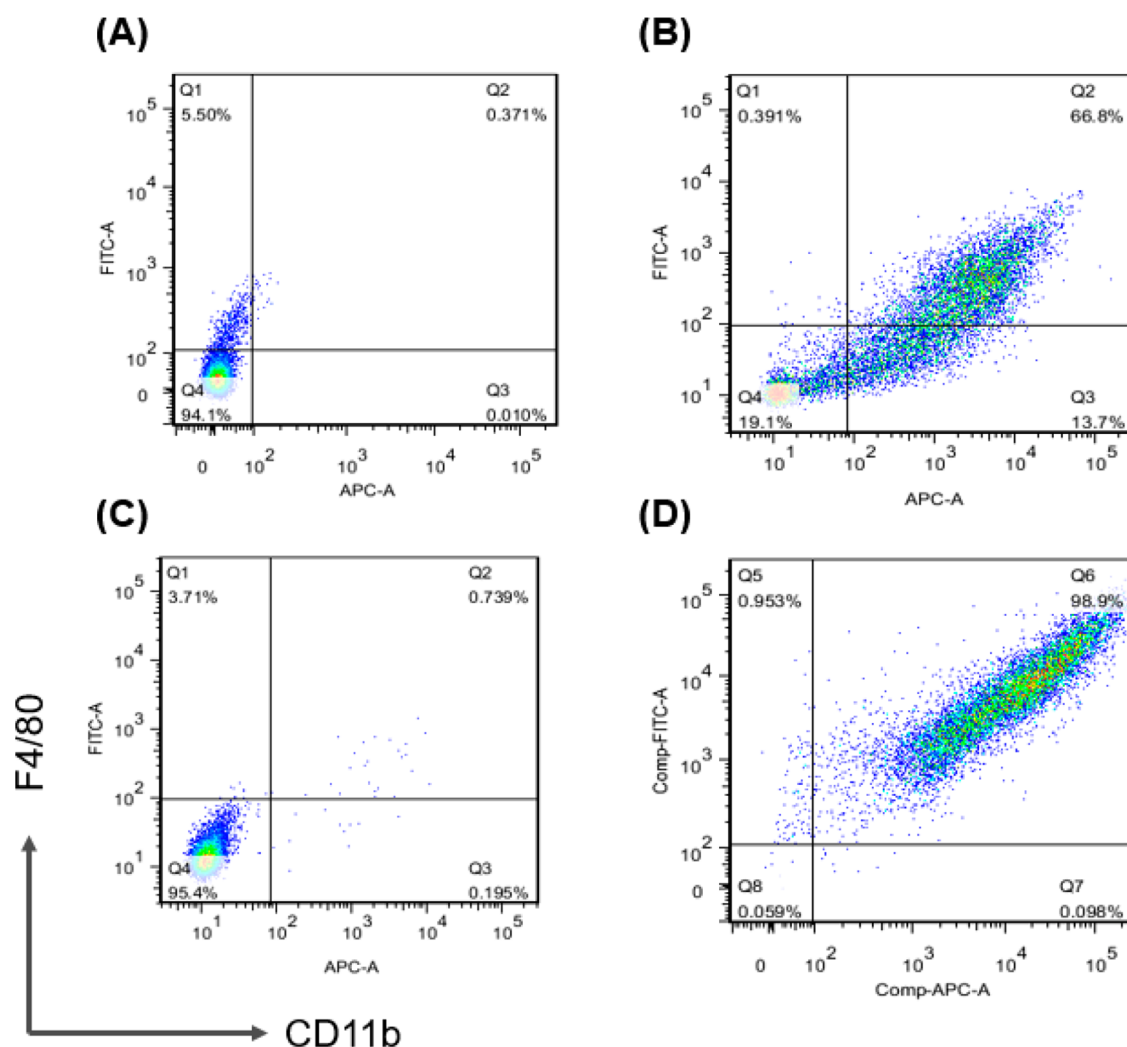


Figure 1. Isolation of splenocytes from the spleens of BALB/c mice and differentiation into M $\Phi$ s. Evaluation of macrophage markers F4/80 and CD11b by FACS analysis. (A, B) 10 days after isolation (A, control; B, antibody stained). (C, D) 25 days after isolation (C, control; D antibody stained).

experiments confirmed that the microrobots could induce an effective anticancer therapy using active targeting and combinational treatment strategy.

## RESULTS AND DISCUSSION

**Preparation and Characterizations of CA-MNPs.** The CA-MNPs were prepared by a chemical coprecipitation technique, resulting in spherical nanoparticles with an average size of approximately 10 nm in diameter, as determined by the transmission electron microscopy (TEM) (Figure S1A). In response to the NIR irradiation (808 nm and 1.5W), the CA-MNP solution temperature quickly reached  $\sim 45$   $^{\circ}\text{C}$ , verifying the NIR laser responsive properties of CA-MNPs (Figure S1B). In addition, experiments with vibrating sample magnetometer (VSM) showed that the magnetic value of the synthesized magnetic CA-MNPs was approximately 50.22 emu/g, confirming their superparamagnetic properties (Figure S1C).

**Preparation and Characterizations of DOX-TSLPs.** Since DOX cannot be loaded directly into primary M $\Phi$ s due to its toxicity, it was incorporated into the liposomes. DOX-TSLPs were synthesized as previously described by our group.<sup>16</sup> Briefly, DOX-TSLPs were prepared by hydrating a

thin lipid film to obtain numerous lamellar vesicles, which were then downsized to nanoscale liposomes by sonication and extrusion (see TEM images of the spherically shaped DOX-TSLPs in Figure S2A).

Size distribution and polydispersity index of the liposomes were measured using the Zetasizer Nano. These measurements demonstrated that DOX-TSLPs had the diameter of approximately 145 nm and a very narrow size distribution with the polydispersity index of 0.13 (Figure S2B). With the active drug encapsulation using ammonium sulfate gradient technique, more than 97% of DOX was successfully encapsulated into the DOX-TSLPs. We performed a drug release test at two pH values, namely, pH 7.4 (resembling blood condition) and pH 5.5 (resembling endosomal condition). At 37  $^{\circ}\text{C}$ , marginal drug was released for both pH conditions during 60 min (Figure S2C). However, at 43  $^{\circ}\text{C}$  (hyperthermia), while cumulative drug liberation was relatively small at pH 7.4, it was  $\sim 65\%$  at pH 5.5 (Figure S2D) in the same time period.<sup>16</sup> The increased releasing rate could be explained as follows: At the pH value of 7.4, the value of the liposomal core and that of the releasing medium was equivalent, thereby inducing no pH gradient. Nonetheless, a pH gradient was induced when the pH value of the releasing

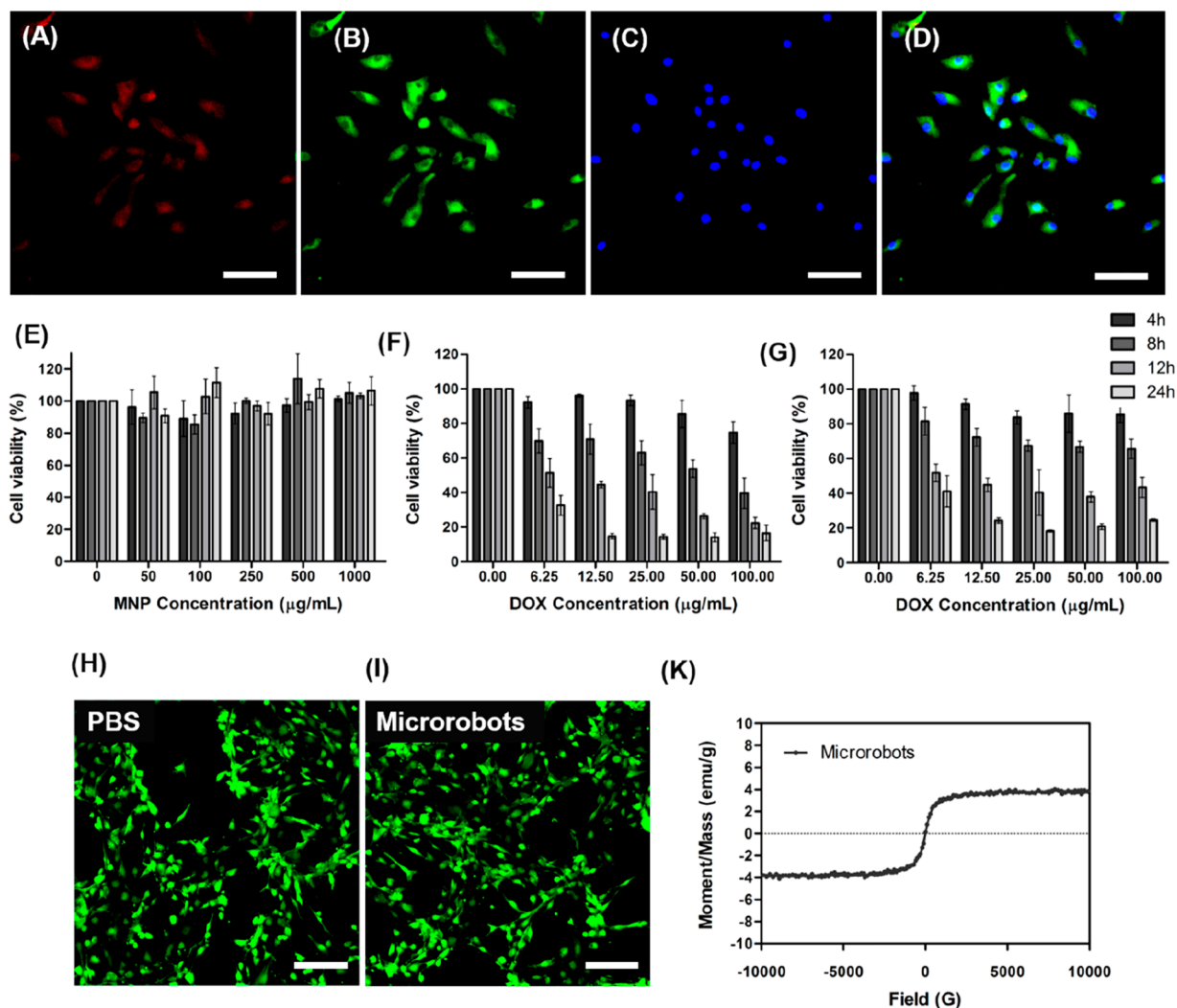


**Figure 2.** *In vitro* characterization of the microrobots. Phagocytosis of MNPs and DOX-TSLPs by macrophages, representative images: (A) DOX-TSLPs; (B) FITC-labeled CA-MNPs; (C) DAPI staining (nuclei); and (D) merged images. Scale bars = 50  $\mu\text{m}$ . Evaluation of cytotoxicity *in vitro*. M $\Phi$ s were incubated with different MNP/DOX concentrations for 4, 8, 12, and 24 h: (E) CA-MNPs; (F) free DOX; and (G) DOX-TSLPs. (H, I) Calcein AM/EthD-1 live/dead cell assay, representative images of M $\Phi$ s treated with (H) PBS or (I) CA-MNPs + DOX-TSLPs (microrobots), scale bars = 100  $\mu\text{m}$ . (K) Magnetization curve of the microrobots. Bars represent SD ( $n = 3$ ).

medium was reduced to 5.5, combining with a hyperthermia temperature of 43  $^{\circ}\text{C}$ , which was greater than the lipid phase transition temperature, thus enabling the collapsing the lipid bilayer of the DOX-TSLPs to trigger the release of DOX. These results verified that hyperthermia, achieved when the coencapsulated CA-MNPs are heated in response to the external NIR laser exposure, could be used to enhance drug release from the liposomal nanocarriers at pH values similar to the endosomal environment. Therefore, it was verified that the prepared DOX-TSLPs had thermosensitive characteristics and would be used to enable on demand drug liberation, thus ensuring the safety of the microrobots from the early drug release from the DOX-TSLPs.<sup>22</sup>

**Isolation of Primary M $\Phi$ s.** Splenocytes isolated from the spleens of mice were cultured in RPMI 1640 supplemented with 10% PBS and 1% penicillin/streptomycin at 37  $^{\circ}\text{C}$  and 5%  $\text{CO}_2$ . Differentiation into M $\Phi$ s was performed by treating cells with 10 ng/mL of colony stimulating factor (M-CSF). The differentiation of M $\Phi$ s was confirmed by the expression of both F4/80 and CD-11b, the M $\Phi$  markers. At day 10, 66.8% of the cells were positive for both markers (Figure 1A,B).

Furthermore, after 25 days, 98.69% of the cells were positive for both CD11b and F4/80 markers (Figure 1C,D), indicating the complete differentiation of splenocytes into M $\Phi$ s. These splenocyte-derived M $\Phi$ s were then used to perform the experiments.

**Preparation of Microrobots.** The microrobots were prepared by coincubating CA-MNPs and DOX-TSLPs with primary M $\Phi$ s. The uptake of the nanoparticles by the M $\Phi$ s was confirmed by confocal laser-scanning microscopy (CLSM). For the purpose of characterization, CA-MNPs were conjugated with fluorescein isothiocyanate (FITC) as previously described, while DOX, due to its intrinsic properties, appeared red at the excitation/emission wavelength of 488/630 nm.<sup>23,24</sup> As a result, both green (FITC) and red (DOX) signals were detected in the cells counterstained with 4',6-diamidino-2-phenylindole (DAPI), therefore, confirming the successful loading of both CA-MNPs and DOX-TSLPs into the M $\Phi$ s (Figure 2A–D). In addition, a biotransmission electron microscope (Bio-TEM) was used to verify the engulfment of the nanoparticles further. We examined Bio-TEM images of different samples of the microrobots harvested

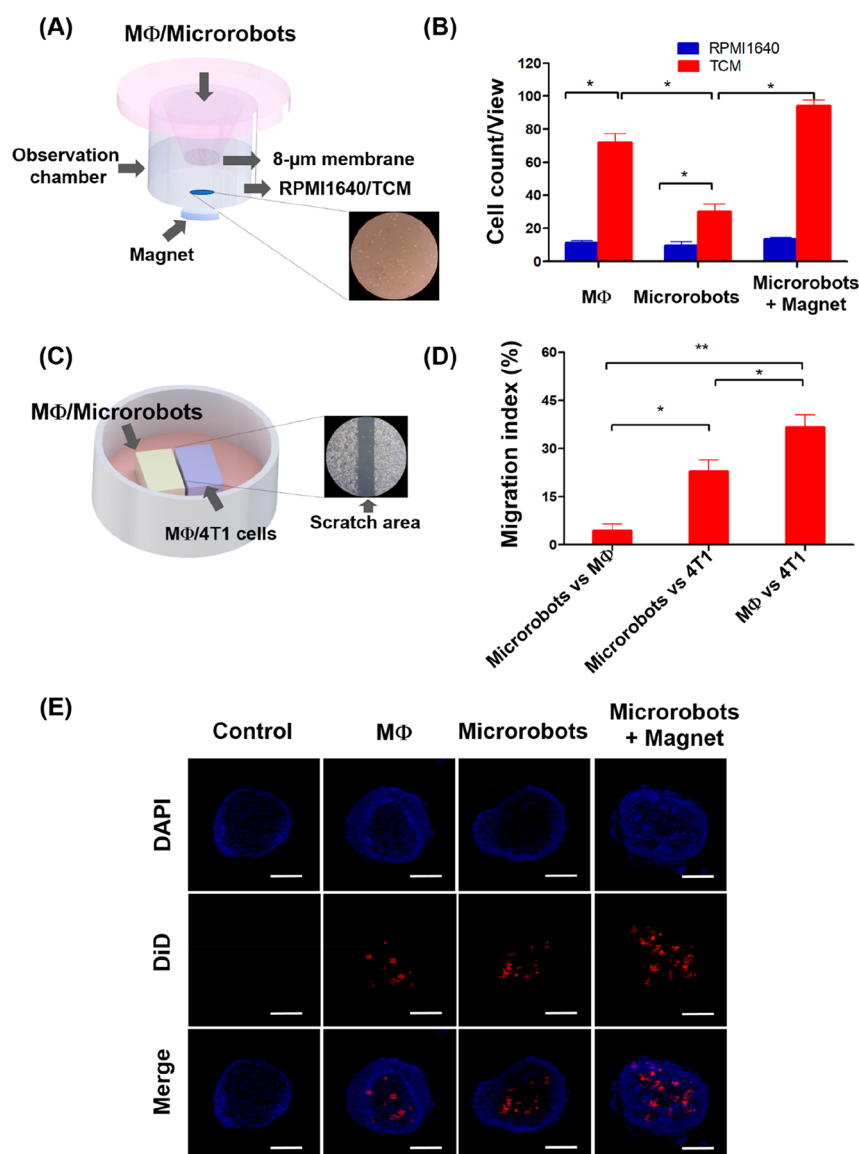


**Figure 3.** *In vitro* tumor targeting evaluation. Tumor targeting, 2D experimental setup: (A, B) Transwell migration assay and migration quantification and (C, D) scratch assay and migration index quantification. (E) Confirmation of microrobot localization inside 4T1-induced spheroids (scale bars = 200  $\mu\text{m}$ ). DAPI (blue) staining indicates cancer cells, and DiD (red) staining indicates microrobots (red signal appearing inside the blue spheroid confirms the successful tumor targeting of the microrobots).

after 8 h of coinubation of CA-MNPs and DOX-TSLPs with M $\Phi$ s and several washing times. Consequently, we observed the colocation of CA-MNPs and DOX-TSLPs in the cytoplasm of the M $\Phi$ s, with their shapes remaining intact in the cellular environment (Figure S3), confirming that the M $\Phi$ s would be protected and maintain their functions for the desired treatment. Next, we verified the cytotoxicity of CA-MNPs, free DOX, and DOX-TSLPs in primary M $\Phi$ s using the thiazolyl blue tetrazolium bromide (MTT) assay. CA-MNPs showed no significant cytotoxicity in M $\Phi$ s at the doses of up to 1000  $\mu\text{g}/\text{mL}$  and the incubation time points of up to 24 h (Figure 2E), indicating that these CA-MNPs were biocompatible with the M $\Phi$ s. However, the cytotoxicity of DOX and DOX-TSLPs in M $\Phi$ s was dose and time dependent, with increased cell death at higher DOX concentrations and longer incubation time points (Figure 2F,G). Compared to DOX-TSLPs, free DOX induced a higher toxicity in M $\Phi$ s,

confirming that free DOX could not be directly loaded into the cells.

Based on the concentrations of both types of nanoparticles, the DOX-TSLP and CA-MNP encapsulation efficiency (EE), and the viability of M $\Phi$ s, we selected the concentrations of 250  $\mu\text{g}/\text{mL}$  for CA-MNPs and 25  $\mu\text{g}/\text{mL}$  for DOX-TSLPs to be used in our experiments. To prepare microrobots, the coinubation time of these nanoparticles with the M $\Phi$ s was set at 8 h. At these conditions, we consistently obtained viable M $\Phi$ s containing both payloads as confirmed by the Calcein AM/ethidium homodimer-1 (EthD-1) live/dead assay and by CLSM (Figure 2H,I). Furthermore, the intracellular content of Fe in  $1 \times 10^7$  microrobots was 319.2  $\mu\text{g}$  (EE of 22.98%), as determined by the inductively coupled plasma atomic emission spectrophotometer (ICP-AES). At the same time, the intracellular amount of DOX was approximately 56  $\mu\text{g}$  in  $1 \times 10^7$  microrobots (EE of 12.45%), as quantified based on the fluorescent intensity of the microrobots in dimethyl sulfoxide

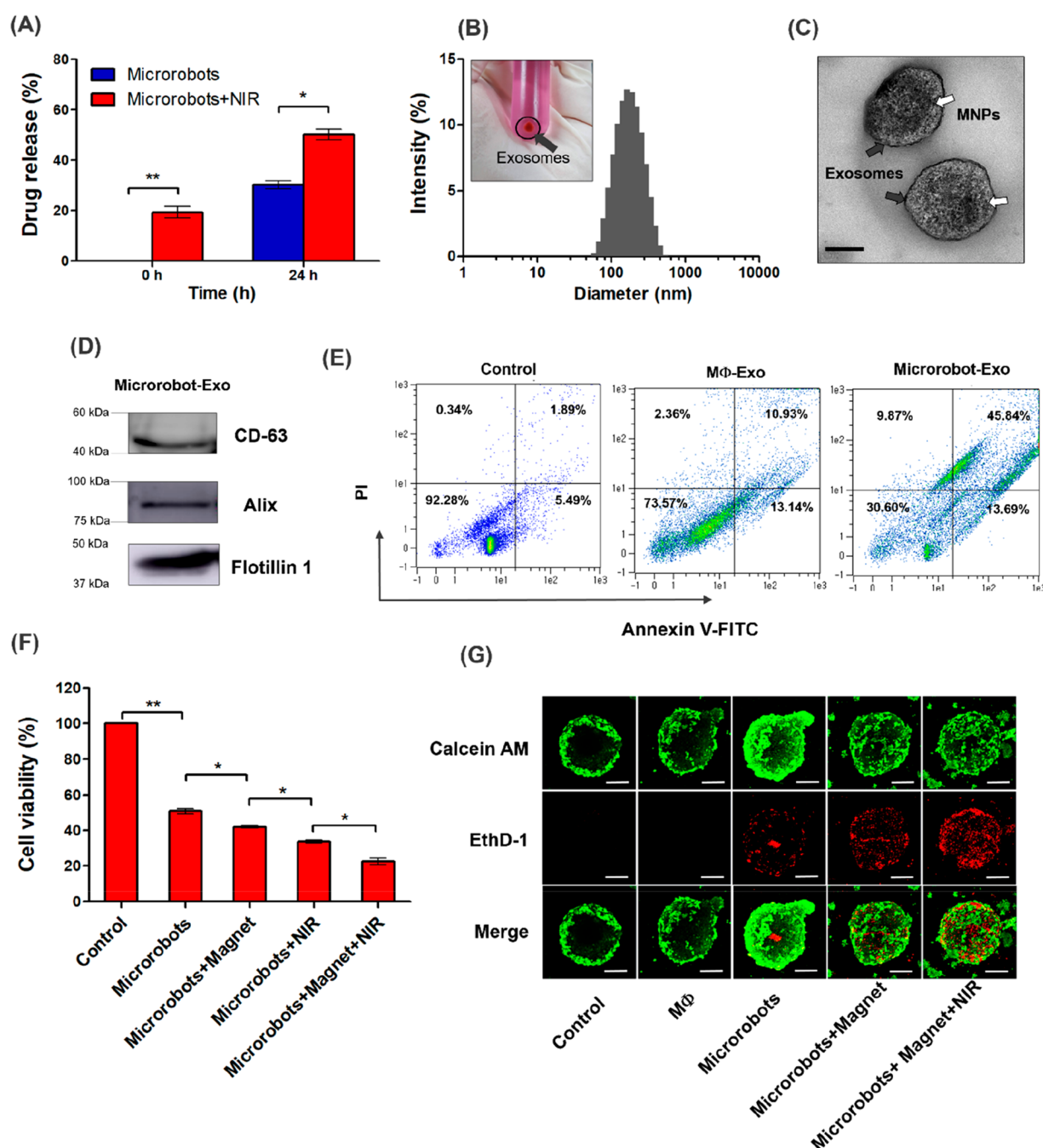


**Figure 4.** *In vitro* characterization of microrobots. (A) Drug release from the microrobots at 0 and 24 h time points, with or without NIR irradiation. (B–E) Evaluation of exosomes released from the microrobots: (B) Size distribution and (B-inset) the image of harvested exosomal pellet after ultracentrifugation; (C) representative TEM image of exosomes, scale bar = 100 nm; (D) Western blotting of exosomal markers, representative blots are shown; and (E) toxicity evaluation of the isolated exosomes in 4T1 cancer cell line using apoptosis detection kit, FACS analysis. (F) Cell viability of 4T1 cells cultured with microrobots was determined using the MTT assay. (G) Cell viability (antitumor ability) of 4T1-induced 3D spheroids was evaluated using the Calcein AM/EthD-1 live/dead cell assay.

(DMSO) calculated using the established DOX standard curve. Figure 2K shows the magnetization curve of the prepared magnetic cellular microrobots, obtained with the VSM using the freeze-dried sample of the microrobots; the magnetization value of the microrobots was approximately 4.07 emu/g.

***In Vitro* Evaluation of Microrobots. *In Vitro* Tumor Targeting.** First, to evaluate the tumor-tropic properties of the developed microrobots in 2D experimental setups, we used Transwell migration as well as scratch assays. For the Transwell

assay, as shown in Figure 3A,B, both primary MΦs and microrobots displayed significantly enhanced chemotactic movement toward the tumor conditioned medium (TCM) compared to the regular culture medium; however, the migration ability of the microrobots was lower than that of primary MΦs, possibly due to the nanoparticle loading. Furthermore, the magnetic field generated by the magnet enhanced the ability of microrobots to move toward the mimicked tumor microenvironment. In the scratch assay, as shown in Figures 3C,D, the microrobots minimally moved

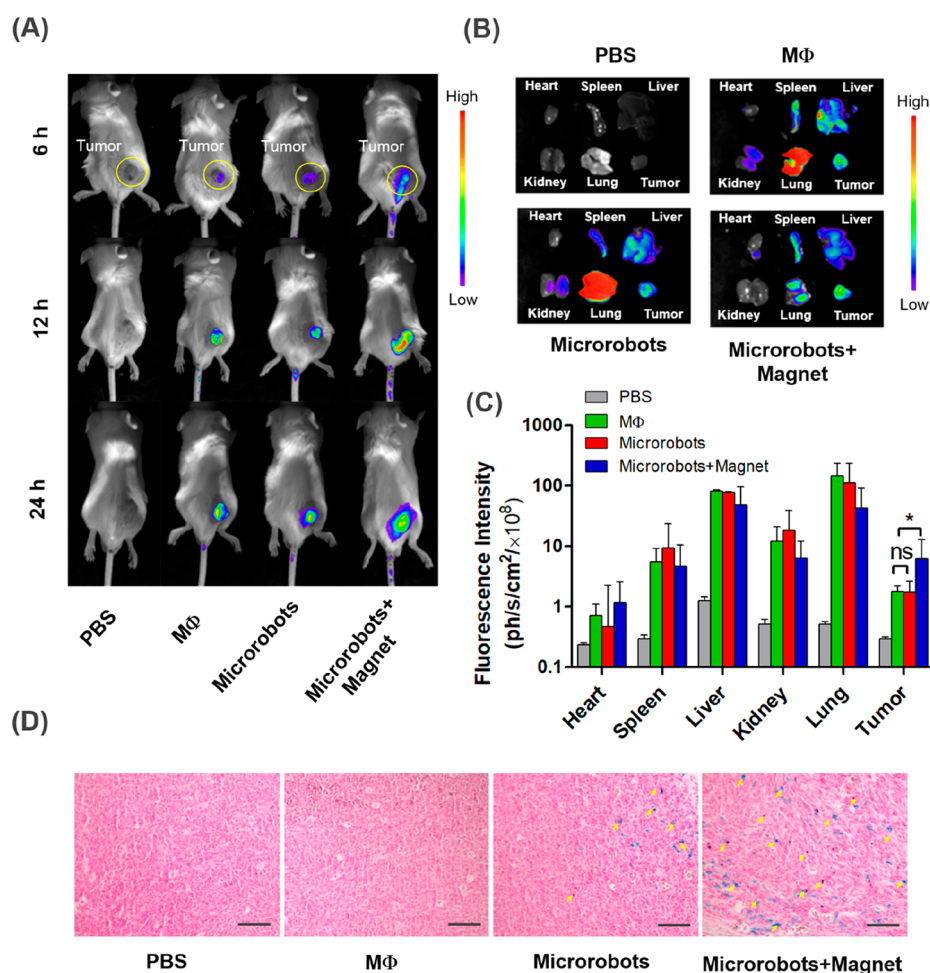


**Figure 5.** *In vivo* characterization of microrobot tumor targeting. (A) Fluorescent images of 4T1 tumor-bearing mice at 6, 12, and 24 h time points after the administration of PBS, MΦ, microrobots, or microrobots + magnet. (B, C) *Ex vivo* fluorescent images of mouse organs with color-coded average fluorescence intensity. (D) Prussian blue staining of the tumors from the mice treated as described in (A); scale bars = 50 μm.

toward primary MΦs; however, their movement was significantly increased during the coculture with 4T1 cancerous cells, the results similar to the Transwell migration assay. Compared to primary MΦs, loaded microrobots still retained their ability to target cancer cells, even though their migration index was decreased.

To further verify targeting of the microrobots to the tumor, we used the 3D *in vitro* model to mimic the hypovascularized lesion microenvironment of the tumor. Tumor spheroids were generated from the 4T1 cancer cells in 96-well cell culture plates with the ultralow attachment surface. First, the MΦs and microrobots were labeled with 1,1'-dioctadecyl-3,3,3',3'-tetramethylindodicarbocyanine (DiD) prior to the incubation with tumor spheroids. Next, microrobots ( $5 \times 10^4$ /well) were added to the wells containing 4T1-induced tumor spheroids and then allowed to infiltrate the tumors for 12 h. After 12 h of incubation, the spheroids were rinsed several times with PBS to remove the microrobots that did not infiltrate the tumor and then stained with DAPI.

As shown in Figure 3E, no red signal was detected in control (PBS only) samples; however, a red signal was detected inside tumor spheroids in all other groups, confirming that MΦs and microrobots had tumor targeting ability and infiltrated the spheroids. Moreover, the application of permanent magnet further increased the number of the microrobots inside the

tumor spheroid, confirming that the magnetic force could be used to enhance the microrobot targeting and infiltration of the tumors. To further verify that the MΦs or microrobots were inside and not on the surface of tumor spheroids, we used a confocal microscope and acquired images at different focal planes of the spheroids. The red signal was detected in all treatment groups, and a higher signal intensity was observed in the microrobots + magnet group (Figure S5). To quantify the tumor targeting ability, we calculated the “penetration index” (PI): the percent of red signal area per total spheroid area. The PIs of MΦs, microrobots, and microrobots + magnet were 7.83%, 7.07%, and 11.39%, respectively (Figure S6A,B).

***In Vitro Drug Release.*** We tested drug release behavior of the microrobots at 0 and 24 h as well as the effect of NIR irradiation on the release. At 0 h, without NIR irradiation, no drug release was observed; however,  $19.23 \pm 2.31\%$  of drug was released from the microrobots upon NIR irradiation. At 24 h,  $30.12 \pm 1.60\%$  and  $50.17 \pm 2.14\%$  of drug was released without and with NIR irradiation, respectively (Figure 4A). In separate experiments, we kept the microrobots in RPMI supplemented with the exosome-depleted FBS for 48 h and then harvested the conditioned media. TEM confirmed the presence of extracellular vesicles, with an average diameter of 159.7 nm as determined by the dynamic light scattering (DLS) method (Figures 4B,C). Furthermore, Western blotting

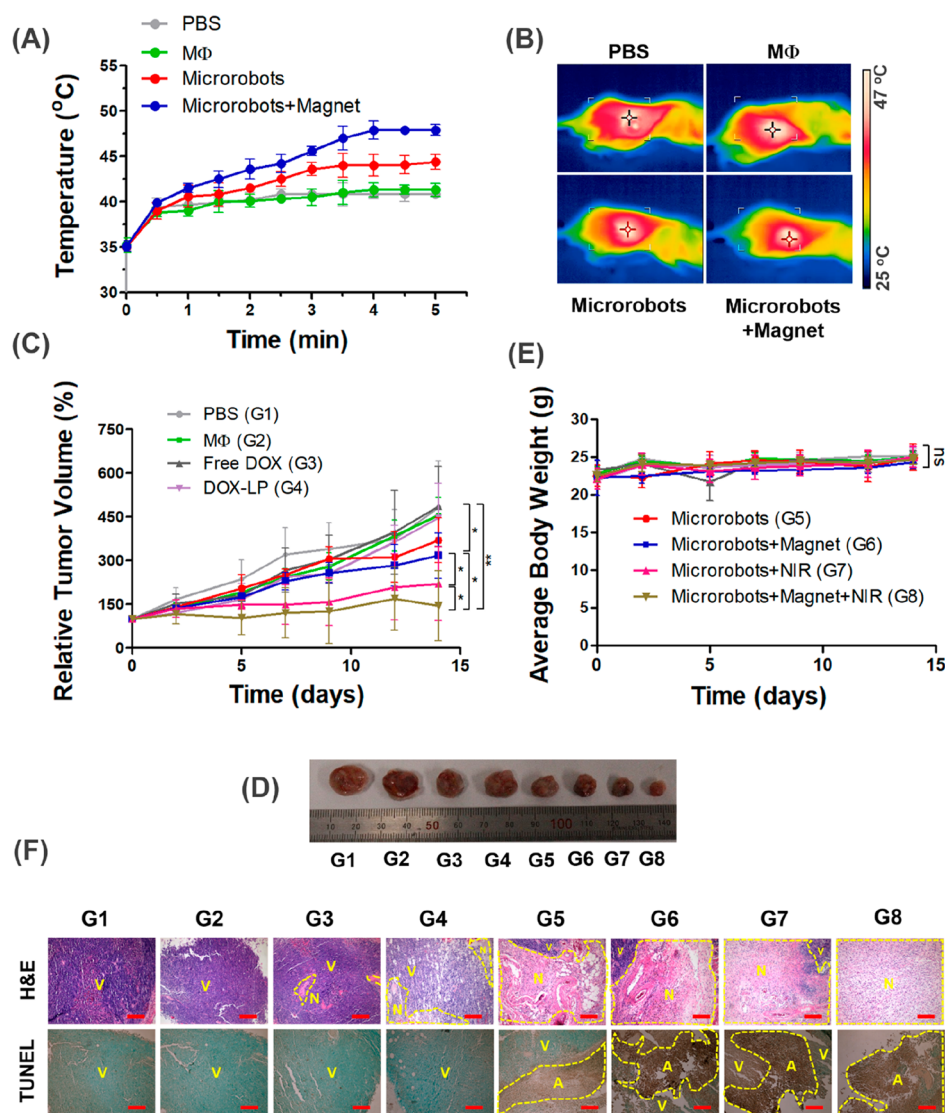


**Figure 6.** *In vivo* evaluation. (A) Temperature change profiles and (B) typical photothermal graphs of 4T1 tumor-bearing BALB/c mice treated with different samples and NIR laser irradiation. (C) Tumor growth profiles of mice after injection of samples; tumor volumes were normalized to their initial sizes (at day 0),  $**P < 0.01$  and  $*P < 0.05$ , bars represent SD ( $n = 5$ ). (D) Typical excised tumors of mice treated with different samples. (E) Body weight profiles of tumor-bearing mice 14 days after injection of samples, bars represent SD ( $n = 5$ ). (F) Histological evaluation of tumors from mice injected with microrobots as indicated. Top row: H&E staining; bottom row: *in situ* apoptosis TUNEL staining: V, viable cells; N, necrotic cells; A, apoptotic cells (scale bars = 50  $\mu\text{m}$ ).

experiments showed that the extracellular vesicles expressed high levels of CD-63, Alix, and Flotilin-1, three well-established exosomal markers, demonstrating that these vesicles were indeed the exosomes released by the microrobots (Figure 4D).<sup>17,25,26</sup> These results indicated that, in addition to DOX, the microrobots also released exosomes, with about 13.91% of DOX released was encapsulated into the exosomes, into the surrounding environment. This may further facilitate cancer drug uptake, since, unlike the artificial nanoparticles, such as liposomes or nanostructured lipid carriers, exosomes express various proteins, including tetraspanins, integrins, and other surfaces adhesion proteins, that would enhance the exosome endocytosis.<sup>17</sup> To verify this, we incubated DOX-TSLPs, microrobot-exos, and microrobot-exos + magnet at an equivalent DOX concentration of 10  $\mu\text{g}/\text{mL}$  with 4T1 cancer cells and compared the cellular uptake after 12 h. FACS data showed that a higher DOX signal was obtained in the cells treated with microrobot-exos in comparison to those treated

with DOX-TSLPs, and the uptake was even enhanced under magnetic field (Figure S4). To examine the ability of the secreted exosomes to induce apoptosis in 4T1 cancer cells, we treated  $1 \times 10^4$  4T1 cells with 100  $\mu\text{g}$  of exosomes released by either the microrobots (microrobot-exos) or M $\Phi$  (M $\Phi$ -exos) for 24 h. The Annexin V-FITC apoptosis detection test demonstrated that microrobot-exos induced apoptosis in 45.84% of the cancer cells compared to 10.93% generated by M $\Phi$ -Exos (Figure 4E), therefore confirming the therapeutic effect of microrobot-exos against cancer cells.<sup>27</sup>

**Cell Viability of 4T1 Cancer Cells in Response to Microrobot Treatment.** To verify the therapeutic efficacy of the developed microrobots *in vitro*, we used 4T1 cancer cells. As shown in Figure 4F, after 24 h, the microrobots reduced 4T1 cancer cells cell viability down to  $50.88 \pm 1.30\%$ , suggesting a significant therapeutic efficacy of the microrobots. The magnetic field further decreased the cell viability to  $42.10 \pm 0.73\%$ , while the exposure to the NIR laser irradiation

critically reduced it to  $33.81 \pm 0.92\%$ . The combined exposure of the magnetic field and the NIR irradiation resulted in only  $25.56 \pm 1.77\%$  viability of 4T1 cells. These experiments confirmed that the microrobots carrying nanoparticle payloads could effectively kill cancer cells, and this therapeutic outcome could be further extended by the external magnetic field and NIR laser irradiation.

**In Vitro Killing Ability of the Microrobots against 4T1 Tumor Spheroids.** We also verified the tumor killing effects of the microrobots against 4T1 tumor spheroids using the Calcein AM/EthD-1 live/dead assay. As shown in Figure 4G, dead cells were detected in the samples treated with microrobots with or without the magnetic field, demonstrating that the microrobots could induce tumor cell death by the drug present in the payloads. Furthermore, the spheroids treated with the microrobots in the presence of magnetic field and exposed to NIR irradiation had the highest number of dead cells. These results could be attributed to the fact that the NIR irradiation increased the temperature of CA-MNPs to induce the enhanced drug release of DOX-TSLPs from the microrobots, resulting in a higher number of dead cancer cells.

**In Vivo Evaluation of the Microrobots. Tumor Targeting and Biodistribution of Microrobots In Vivo.** To investigate the tumor targeting of the microrobots *in vivo*, we intravenously injected tumor-bearing mice with  $5 \times 10^6$  of DiD-labeled M $\Phi$  or microrobots. A magnet was attached to the tumor of each mouse in the microrobots + magnet group to evaluate the contribution of magnetic targeting. Mice injected with PBS were used as controls. Images of the mice were captured at 6, 12, and 24 h postinjection using an *in vivo* imaging system (IVIS) (Figure 5A). The results showed that the DiD fluorescence signal gradually increased over the evaluated time periods, suggesting the ability of M $\Phi$ s and the microrobots to move toward tumors. Furthermore, in the microrobots + magnet group, the DiD signal in the tumors was markedly increased, confirming the role of magnetic field in enhancing the movement of the microrobots toward tumors *in vivo*. Moreover, the *ex vivo* images of the mouse organs showed that, in addition to tumors, the M $\Phi$ s and microrobots were also detected in the lung, spleen, and liver (Figure 5B,C). Interestingly, the presence of the magnetic field reduced the DiD signal in the lungs and increased the signal in the tumors, thus further verifying that the microrobots were actively navigated more effectively to the tumor sites. These results were also confirmed by the Prussian blue staining of the tumor tissues (Figure 5D). Specifically, almost no blue signal was detected in the tumor tissues of the mice treated with PBS and M $\Phi$ . A stronger positive staining was observed in the tumor tissues of mice treated with microrobots (see yellow arrows). More importantly, a critical higher signal of Fe was observed and distributed in the large portion of the tumor tissue (yellow arrows). In addition, we investigated the blood clearance rate of the microrobots when intravenously injected into the tumor-bearing mice. For comparison, we prepared three groups of mice, namely M $\Phi$ , the microrobots, or microrobots + magnet. The half-life of each injected sample was determined based on the obtained relative blood fluorescence intensity (FI) from the collected blood (Figure S7). M $\Phi$  and the microrobots had comparable half-life values of 9.14 and 8.12 h, respectively, while the microrobots + magnet had a half-life of 4.59 h. The shorter half-life of this group may be attributed to the role of the magnetic targeting that attracted the microrobots to the tumor sites, thus reducing the blood

circulation of the microrobots. These results further confirmed that the enhanced tumor targeting of the microrobots could be achieved with an external magnetic field.

**Photothermal Effect.** Next, we investigated the response of the microrobots to the NIR laser irradiation. In these experiments, mice were injected with  $5 \times 10^6$  microrobots into the tail vein. In the microrobots + magnet group, permanent magnets were attached to the mice for 12 h after the injection. The control groups were injected with PBS or  $5 \times 10^6$  M $\Phi$ s. Laser irradiation (1.5 W, 5 min) was performed at 24 h postinjection. Thermal changing profiles and representative thermal images of the mice from different treatment groups are shown in Figure 6A,B. After NIR irradiation, the change of tumor temperatures of the mice treated with PBS (control) or M $\Phi$  was minimal, whereas the temperature of the microrobot-injected mouse tumors increased up to  $44.4^\circ\text{C}$  ( $\Delta T = 9.3^\circ\text{C}$ ) after 5 min. Furthermore, the average temperature of the tumors of the mice exposed to the magnetic field rose sharply to  $47.9^\circ\text{C}$  ( $\Delta T = 12.8^\circ\text{C}$ ). These temperature increases may further assist drug release from the liposomes and, therefore, could enhance tumor ablation. The rapid change in the tumor temperature could be caused by the effective infiltration of microrobots into the tumors, especially under the influence of the magnetic field induced by the magnets.

**In Vivo Therapy.** Next, we tested the *in vivo* anticancer therapeutic efficacy of these microrobots. Mice were divided into eight groups ( $n = 5/\text{group}$ ) and injected with PBS, M $\Phi$ , free DOX, DOX-TSLPs, microrobots, microrobots + magnet, microrobots + NIR, and microrobots + magnet + NIR. All groups were injected once during the treatment period. First, we measured relative tumor volumes in each group (the final tumor volume was normalized to the initial one). As shown in Figure 6C,D and Figure S10, the treatment with M $\Phi$ , free DOX, and DOX-TSLP did not show any significant inhibition of tumor growth compared to the PBS control group. At the same time, all groups treated with the microrobots showed significant delay in the tumor growth compared to the control. Mice injected with the microrobots and exposed to the magnetic field had further reductions in the tumor growth. Finally, the group treated with microrobots, magnetic field, and NIR irradiation displayed the highest inhibition of tumor growth. At the same time, no specific weight loss was observed in all treatment groups, verifying that all samples showed no systemic toxicity in mice during the treatment (Figure 6E). In a separate experiment, on day 7 postinjection of various samples, we euthanized the mice and collected blood and major organs for further evaluation. We examined the hepatic indicators such as alanine aminotransferase (ALT), aspartate aminotransferase (AST), alkaline phosphatase (ALP), and an indicator for kidney functions: blood urea nitrogen (BUN). As a result, all parameters were in the normal ranges in comparison with the control, thereby further verifying the favorable *in vivo* biocompatibility of the prepared microrobots (Figure S8). Our observations were more supported by the histological analysis (H&E) of the mouse major organs, which also confirmed the absence of toxicity in the organs that were examined (Figure S9). Furthermore, the H&E and terminal deoxynucleotidyl transferase (TdT) dUTP nick-end labeling (TUNEL) analysis of tumor tissues showed the absence of apoptotic cells in the tumor tissues of the PBS treated group; however, extensive tissue damage and presence of apoptotic cells were detected in the groups treated with microrobots

(Figure 6F). In a separate experiment, we have observed the survival data of the mice treated as above. As a result, Kaplan–Meier survival analysis revealed that 60% of the mice in the microrobots + magnet + NIR treatment group survived until day 50 post-treatment (Figure S11). These results further confirmed the advantage of using these microrobots, together with magnetic targeting and NIR irradiation, to effectively destroy tumor cells.

It is widely accepted that targeting nanomedicines to tumors would improve the diagnosis and therapeutic outcomes, since the nanoscale-sized medicines could easily penetrate into the tumor due to its enhanced permeability and retention effect. However, it was recently published that only approximately 0.7% of the initial injection dose reached the targeted site.<sup>28</sup> This also means that over 99% of the drug ended up off-target, in other organs, potentially causing severe side effects. Therefore, there is an urgent need to develop a more effective way to deliver drugs. MΦs, as a part of the mononuclear phagocytic system, possess strong phagocytic activity as well as an intrinsic ability to home tumors, sometimes making up to 70% of the whole tumor mass.<sup>29</sup> These properties promoted the development of MΦ-based nanomedicine DDSs to treat tumors with promising outcomes.<sup>30–35</sup> However, to develop these systems, commercial macrophage cell lines were usually adopted, even though these cells could be recognized as foreign objects and evoke immune responses when injected into an animal model.<sup>36</sup> In the present study, we developed MΦ-based microrobots using primary MΦs from BALB/c mice, loaded with CA-MNPs and DOX-TSLPs, and injected back into the same mouse strain, therefore, reducing the possibility of an immune response in these animals. As a result, the therapeutic outcomes could be easily interpreted, adding valuable scientific evidence to future clinical applications. In addition, the NIR laser has been recently used in MΦ-based DDSs to enable an effective photothermal antitumor cancer therapy. So far, plasmonic nanoparticles, such as gold nanoparticles or gold nanospheres, have been commonly used in these systems; however, these nanoparticles do not allow an external control of the DDS.<sup>14,15,37</sup> For that purpose, remote magnetic fields offer a convenient and effective strategy, and have already been widely used in biomedical applications.<sup>38–43</sup> Therefore, to combine the use of both NIR and the external magnetic field in a single platform, we synthesized biocompatible CA-MNPs, which are not only NIR responsive but also have superparamagnetic properties, therefore, offering the feasibility of an external magnetic control.<sup>44</sup> Furthermore, the average size of 100–200 nm would facilitate the uptake of TSLPs by the MΦs, high DOX loading efficiency, while the thermosensitive properties would allow spatiotemporal drug release upon the NIR laser irradiation, thus minimally reducing an early premature release before reaching the target site.<sup>45</sup> In this study, we showed that in addition to free DOX molecules, the microrobots also released exosomes with a high therapeutic effect, as tested on the cancer cells. Therefore, with the dual targeting functions combined on-demand drug release from the MΦ-based microrobots, only a subtherapeutic dose of DOX of 1.25 mg/kg with single injection was used with excellent outcomes, thus suggesting the advancement of our proposed MΦ-based microrobotic platform.<sup>46</sup> Although the principle technology proposed in this study focuses on primary MΦs isolated from mouse spleens, it can be applied to many types of cells (for instance, stem cells and natural killer cells) to target a given superficial solid tumor,

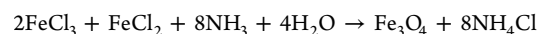
as long as these cells could be engineered to load or attach MNPs and chemotherapeutic nanoparticles. Ideally, our final strategy would be to isolate macrophages from a cancer patient, *in vitro* engineer the cells with therapeutic payloads (including MNPs), and then infuse the engineered cells back into the patient. Instead of a permanent magnet, as used here in a proof-of-principle study, a multifunctional electromagnetic actuating system with versatile controllability could be used to generate a strong and directional electric field to guide the cells to the target tissues.<sup>47</sup>

## CONCLUSION

In summary, we isolated mouse splenocytes, differentiated these cells into MΦs, and injected the cells back into the mice after engineering cells with payloads. In addition, the use of thermosensitive liposomes containing DOX with CA-MNPs allowed us to perform multimodal treatments of tumors, resulting in enhanced therapeutic outcomes of the treatments, with a subtherapeutic dose of the drug and only one-time injection. This strategy would reduce the burden for some of the patients, while enhancing the therapeutic efficacy of the treatments. In addition, we have shown that the use of an external magnetic field, a noninvasive technique, in combination with the NIR laser irradiation would lead to a significant enhancement of the therapeutic outcomes.

## METHODS

**Preparation CA-MNPs and DOX-TSLPs.** CA-MNPs were synthesized by a chemical coprecipitation method based on a previously published protocol with minor modifications using the chemical reaction below:



Briefly,  $\text{FeCl}_3$  and  $\text{FeCl}_2$  (Sigma-Aldrich, St. Louis, MO) were prepared in DI water, heated to 80 °C, and mixed well with a mechanical stirrer in a three-necked flask. Next, 40 mL of 25%  $\text{NH}_4\text{OH}$  was added to the mixture through a glass syringe connected to one of the necks. After MNPs were formed, they were washed several times with DI water, dispersed in DI water, and 10 mL of CA (0.5 mg/mL) was added to the mix. The temperature was adjusted to 90 °C and the mixture was then stirred for 60 min. Finally, the CA-MNPs were washed several times with DI water, harvested with a magnet, and then were lyophilized for 48 h under vacuum (FreeZone 2.5, Labconco, Kansas City, MO, USA). The lyophilized MNPs were stored at –20 °C until further use.<sup>48</sup>

The DOX-TSLPs were prepared by a hydration with sonication and extrusion method for the nanoscale size reduction as previously described.<sup>16</sup> Briefly, dipalmitoyl-*sn*-glycero-3-phosphocholine (DPPC, 34 mg) and 1-myristoyl-2-stearoyl-*sn*-glycero-3-phosphocholine (MSPC, 6 mg) (Avanti Polar Lipids, Alabaster, Alabama) were mixed with chloroform/methanol (9:1, volume:volume) in a glass pear-shaped flask. After thoroughly dissolved, the solvents were evaporated under vacuum using a rotary evaporator (Büchi R-300, Flawil, Switzerland). During the evaporation, the temperature of the water bath was kept at 50 °C. The resulting thin film on the surface of the flask remained under vacuum overnight to ensure a complete removal of remaining solvents. Next, the thin film was hydrated with 2 mL of 250 mM ammonium sulfate solution at 50 °C in the water bath for 30 min, forming multiple lamellar vesicles.<sup>49</sup> The obtained lipid vesicles were briefly sonicated with a probe sonicator (VC750, Sonics & Materials, Newtown, CT) to reduce the size and then extruded several times through polycarbonate membranes using a small size extruder (Avanti Polar Lipids, Alabaster, Alabama) to make nanoscale TSLPs. Next, the liposomes in the solution were subjected to gel filtration using Sephadex G25 column pre-equilibrated with phosphate buffered saline (PBS). DOX was encapsulated into the

liposomes utilizing the ammonium sulfate gradient technique as previously described.<sup>49</sup> The nonencapsulated DOX was removed by gel filtration as described above. Finally, the purified DOX-TSLPs in PBS were stored at +4 °C until further use.

**Characterization of CA-MNPs and DOX-TSLPs.** We characterized the surface morphologies of CA-MNPs and DOX-TSLPs using TEM (TECNAI F20 ST, FEI Company, Hillsboro, OR). The size of the DOX-TSLPs was measured using the Zetasizer Nano (Malvern, UK), while the size of the CA-MNPs was determined by quantifying the TEM images using the ImageJ software (NIH). Magnetization curves of CA-MNPs and the microrobots were obtained using VSM (Lake Shore Cryotronics 7404, Westerville, OH). DOX-TSLP drug release was determined by measuring the fluorescent intensity of DOX in the supernatants.

#### Isolation of Primary MΦs from the Spleens of BALB/c Mice.

The isolation of primary MΦs from murine spleen was performed as described in the previously published protocol.<sup>50</sup> All animal experiments were performed in accordance with the Guidelines and approved by the Animal Care and Use Committee of Chonnam National University (Korea). Six-week old BALB/c mice were purchased from Orient Bio Inc. (Seoul, Korea). For the isolation of primary MΦs, mice were sacrificed using CO<sub>2</sub> inhalation. Spleens were dissected out and then passed through a 70 μm nylon strainer. The red blood cells were removed using the cell lysing buffer (BD Pharm Lyse, 555899) to obtain a single splenic cell suspension. The cells were maintained in RPMI 1640 cell culture media supplemented with 10% FBS and 1% penicillin-streptomycin (WELGENE, Gyeongsangbuk-do, Korea). To induce MΦ differentiation, cells were treated with macrophage colony stimulating factor (10 ng/mL) (M-CSF, GenScript, Piscataway, NJ, USA). To confirm MΦ differentiation, the expression of CD11b and F4/80, the markers of the MΦs, was assessed using fluorescent actuated cell sorting (FACS) analysis. Briefly, the MΦ suspension was washed with FACS buffer (1% BSA in PBS), the cells were incubated with anti-CD11b-APC (130-113-802; Miltenyi Biotec, Germany) and anti-F4/80-FITC (130-117-509; Miltenyi Biotec, Germany), and analyzed using a MACSQuant VYB flow cytometer (MACS Miltenyi Biotec, Auburn, CA, USA).

**Preparation of Microrobots.** Primary F4/80- and CD11b-positive MΦs were continuously maintained in the RPMI 1640 cell culture media supplemented with 10% FBS, 1% penicillin-streptomycin, and 10 ng/mL M-CSF in 6-well cell culture plates. Upon reaching confluence (~5 × 10<sup>6</sup> cells/well), the cells were incubated with DOX-TSLPs and CA-MNPs for 8 h. Next, the media were removed, and the cells were washed several times with PBS to remove the nanoparticles that were not taken up by the cells. The obtained microrobots were then harvested using a cell scraper.

**Characterization and Evaluation of the Microrobots.** The successful loading of nanoparticles into primary MΦs was verified using CLSM (TCS SPS/AOBS/Tandem, Leica, Wetzlar, Germany). For this purpose, the CA-coated MNPs were conjugated with fluorescein. At 480 nm excitation and 630 nm emission, DOX would appear red, while the fluorescein-conjugated MNPs would appear green. DAPI (Thermo Fisher Scientific, Waltham, MA, USA) was used as a counterstain to identify the nuclei.<sup>51</sup> In addition, Bio-TEM was also used to verify the engulfment of the nanoparticles into the macrophages. In brief, after incubation of CA-MNPs and DOX-TSLPs into the macrophages for 8 h, the cells were washed several times to remove unbound nanoparticles. The obtained microrobots were then fixed with glutaraldehyde (GA, 2%) at 4 °C overnight. After that, GA was replaced by PBS, followed by postfixation treatment with OSO<sub>4</sub> (1%) solution for 2 h at 4 °C. Then, the microrobots were washed three times with PBS. Next, the microrobots were dehydrated with ethanol (50, 70, 90, 95, and 100%) and ethanol:acetone (1:1; v/v) solutions for 20 min in each solution. After a dehydration series in acetone solutions, the microrobots were treated with acetone:epoxide resin (1:2; v/v) overnight, followed by immersing in pure epoxide resin and allowed to polymerize. After that, the specimens were cut into ultrathin (80–100 nm) slices using ultramicrotome with a

diamond knife. The slices were then placed on carbon-coated grids and observed under TEM equipment.<sup>20</sup>

To quantify the intracellular MNPs, 1 × 10<sup>7</sup> microrobots were prepared in nitric acid (HNO<sub>3</sub>, 70%) solution and heated at 80 °C for 4 h, allowing the intracellular MNPs to be converted into ferric ions. After diluting with DI water (1/10, v/v), the iron amount was analyzed and determined using ICP-AES (PerkinElmer OPTIMA 8300, Wellesley, MA, USA) at a 238.204 nm wavelength. The intracellular DOX content was determined by dissolving the 1 × 10<sup>7</sup> microrobots in DMSO, and the fluorescent intensity was measured using a multimode microplate reader (Varioskan Flash, Thermo Scientific, Waltham, CA, USA). The amount of DOX was then estimated by the fluorescent intensity of the microrobot lysates based on a prepared DOX standard calibration curve.<sup>52</sup>

**Cancer Cell Culture.** 4T1 cells were purchased from the American Type Culture Collection (Manassas, VA, USA). Cells were maintained in DMEM supplemented with 10% FBS and 1% antibiotic solution in a humidified incubator at 37 °C in 5% CO<sub>2</sub>.

**In Vitro Tumor Targeting with 2D Experimental Setup.** For the Transwell assay, 5 × 10<sup>3</sup> MΦs/microrobots were suspended in the upper chamber of the Transwell insert equipped with an 8 μm pore PC membrane in complete culture medium (RPMI 1640, supplemented with 10% FBS and 1% penicillin-streptomycin), while the lower chamber contained either TCM from 4T1 cancer cells (containing 20% FBS) or complete culture medium as a control. The use of TCM in this experiment would allow us to mimic the tumor microenvironment that would contain chemo-attractants and/or growth factors secreted by the cancer cells and possibly involved in the migration of MΦs.<sup>52</sup> For one of the experimental groups, a magnet was placed underneath the bottom of the well to evaluate the magnetic targeting ability of the microrobots. In the scratch assay, 7 × 10<sup>4</sup> MΦs/microrobots were plated in one reservoir of the Ibidi insert (81176, Ibidi, Gräfelfing, Germany), while MΦs/4T1 cells were loaded in the other reservoir. The inserts were then removed after 24 h. Then, the cellular migration toward the 4T1 cells was allowed in 8 h. In this experimental setup, the migration index was calculated as the percent of postcell movement area per the original scratch area.<sup>52</sup>

**In Vitro Tumor Targeting with 3D Tumor Spheroids.** The tumor-targeting ability of the microrobots was evaluated using the breast cancer 4T1 cell line. To generate an *in vitro* solid tumor model, 4T1 3D tumor spheroids (with an average diameter of approximately 600 μm) were induced using ultralow attachment plates. After the spheroids were formed, the used media were discarded, and 100 μL of DMEM solution containing the MΦs loaded with nanoparticles was added to the wells. First, MΦs were labeled with DiD (Thermo Fisher Scientific). Next, the spheroids were treated with MΦs, microrobots (5 × 10<sup>3</sup> MΦs/microrobots per well), and microrobots with a magnet attached to the bottom of the well. The spheroids treated with PBS were used as a control. Spheroid penetration was allowed to proceed for 12 h. The media were then removed, and the spheroids were rinsed three times with PBS. Finally, the spheroids were fixed in 4% paraformaldehyde, stained with DAPI, and observed using confocal microscopy.

**In Vitro Cytotoxicity Test.** MTT assays were used to evaluate the toxicity of the MΦs treated with various concentrations of MNPs, free DOX, and DOX-TSLPs at different incubation time points. First, the MΦs were rinsed three times with PBS, and 10 μL of MTT (Sigma-Aldrich (St. Louis, MO, USA)) in 100 μL of DMEM was added to each well. After 3.5 h, the used media were replaced with an equal volume of DMSO solution. The absorbance at 570 nm was measured by the multimode microplate reader.

Next, the *in vitro* antitumor efficacy of the microrobots in 4T1 cancer cells was also verified. Briefly, 1 × 10<sup>4</sup> 4T1 cells/well were seeded in 24-well plates and incubated for 24 h. The cells were then treated with 1 × 10<sup>4</sup> MΦs/microrobots with/without the NIR exposure. Cell viability after 24 h of incubation was calculated as described above.

To investigate the antitumor activity of the microrobots, the 4T1-induced tumor spheroids were treated with the microrobots. NIR laser (1.5 W, 808 nm, PSU-W-FC laser power supply, Changchun

New Industries Optoelectronics Technology) was used to further enhance the therapeutic efficacy of the microrobots against the tumor, allowing effective multimodal treatment of the tumors. Briefly, we treated the tumor spheroids with either PBS or microrobots for 12 h to allow tumor infiltration of the microrobots. A magnet was attached at the bottom of the well for the magnetic targeting group. The spheroids were then washed with PBS to remove free microrobots. Next, the spheroids were exposed to NIR irradiation for 5 min and incubated for 24 h before stained with Calcein AM/EthD-1 kit (L3224, Thermo Fisher Scientific) following the manufacturer's protocol.

**Animal Model.** BALB/c mice (Orient Bio Inc., Seoul, Korea) was used in these experiments as previously described.<sup>53</sup> All animal experiments were carried out in accordance with and approved by the Animal Care and Use Committee of Chonnam National University, the Republic of Korea. Breast tumors were induced by subcutaneously injecting  $1 \times 10^6$  4T1 cells suspended in 100  $\mu$ L of PBS into the right flank of each mouse. The tumors were formed at around day 10 postinjection, with an average size of approximately 100 mm<sup>3</sup>.

**Tumor Targeting and Biodistribution of the Microrobots *In Vivo*.** The tumor-bearing mice were anesthetized and intravenously injected through a tail vein with  $5 \times 10^6$  M $\Phi$ s or the microrobots, which were previously labeled with 0.25 mg/mL DiD (Thermo Fisher Scientific) solution, as specified in the manufacturer's instructions. For the control group, mice were injected with the same volume of PBS. For the magnetic targeting group, after the injection, a permanent magnet was attached to the tumor of each mouse with a surgical tape. At 6, 12, and 24 h postinjection, the DiD signal from the M $\Phi$ s and the microrobots was detected at the excitation/emission wavelength of 644/665 nm using the IVIS system (LB 983, NightOWL II, Berthold Technologies, Germany).<sup>54</sup> To observe the *ex vivo* biodistribution of DiD signal in major organs, the mice were sacrificed, the organs were excised, and the images were captured using the same wavelength of the same system. The mean fluorescence intensity of the organs was determined using indiGo Software supplied with the equipment.

**Blood Circulation Time.** We measured blood circulation time by intravenously injecting DiD labeled  $5 \times 10^6$  M $\Phi$ s or the microrobots into the mice ( $n = 3$  per group). At each time point of 3 min, 1, 2, 4, 8, 24, 36, 48, and 96 h, 20  $\mu$ L of blood was collected *via* capillary tubes with heparinized coatings (Kimble Chase Life Science and Research Products, Vineland, New Jersey, USA) and was immediately mixed with 20  $\mu$ L of 0.2% ethylenediaminetetraacetic acid (GenDEPOT, Barker, TX, USA) at pH 7.4 for anticoagulation of the blood. After that, the DiD signal from the blood was detected using the IVIS system, from which the relative FI was quantified, as mentioned previously. Then, the blood clearance rate (half-life) was determined accordingly.<sup>55</sup>

In the next set of experiments, the animals were randomly divided into eight groups ( $n = 5$  per group), anesthetized, and intravenously injected with PBS, M $\Phi$  only, free DOX, DOX-TSLPs, microrobots, microrobots + magnet, and microrobots + magnet + NIR (CA-MNPs 7.25 mg/kg; DOX 1.25 mg/kg). NIR laser irradiation (808 nm, 1.5 W) was performed for 5 min at 24 h postsample injection. Tumor size was monitored and measured every 2 or 3 days for 14 days using a digital caliper. Tumor volume was determined using the following formula:  $L \times W^2/2$ , where  $L$  and  $W$  are the longest and shortest dimension of a tumor, respectively.<sup>44,53</sup>

**Survival Rate Evaluation.** In a separate experiment, eight groups of mice ( $n = 5$  per group) were prepared and treated as mentioned previously. The animals were checked daily, and the overall survival data were documented until day 50.<sup>56</sup>

***In Vivo* Thermal Imaging.** The 4T1 tumor-bearing mice were intravenously injected with PBS, M $\Phi$ s only, microrobots, or microrobots + magnet and then exposed with NIR light (808 nm, 1.5 W) for 5 min. The change of the tumor temperature was measured using an infrared (FLIR) camera.<sup>57,58</sup>

**Blood Biochemistry.** Mice were treated with different samples. On day 7 postinjection, the mice were euthanized, and the blood (1 mL per mouse) was collected. The whole blood was then centrifuged at  $2000 \times g$  in 10 min at 4  $^{\circ}$ C, and the serum was collected. Hepatic

indicators such as ALT, AST, and ALP and indicators for kidney functions BUN were determined from the serum using an automated dry chemistry analyzer (DRI-CHEM 700i, Fuji Film, Japan).<sup>59</sup>

**H&E Examination.** For histological examination, the mice were sacrificed on day 7 postinjection, and the major organs, including the heart, spleen, liver, kidneys, lungs, and tumors, were dissected, fixed in 4% PFA, and embedded in paraffin before further use. The tissue sections (5  $\mu$ m of thickness) were cut using a microtome and mounted onto adhesive glass slides. The sectioned tissues were then stained with H&E following a standard protocol and analyzed under a microscope.<sup>52</sup>

**Exosome Isolation and Analysis.** In a 10 cm cell culture plate,  $5 \times 10^6$  M $\Phi$ s were seeded. After overnight incubation, the cells were loaded with CA-MNPs and DOX-TSLPs as described previously. After 8 h of cocultivation, the cells were washed at least five times with PBS to remove the nonphagocytosed nanoparticles and then incubated with fresh PRMI-1640 supplemented with 10% of exosome-depleted FBS and 1% penicillin and streptomycin. The conditioned media were collected after 48 h. The exosomes from the collected media were isolated using the differential ultracentrifugation method as previously described with minor modifications.<sup>60</sup> Briefly, 10 mL of the media was sequentially centrifuged at  $1000 \times g$  for 10 min and then  $10,000 \times g$  for 30 min to remove the cell debris and dead cells, while the supernatant was retained. Next, the supernatant was centrifuged at  $100,000 \times g$  for 90 min at 4  $^{\circ}$ C using an ultracentrifuge (CP100NX, Himac, Koki Holdings, Tokyo, Japan). The exosomal pellet was resuspended in PBS for the analysis. The protein concentration of exosomes was measured using the bicinchoninic acid (BCA) protein assay using the exosomal lysate obtained by radioimmunoprecipitation buffer (RIPA, P8100, GenDEPOT). Samples and standards (25  $\mu$ L) were pipetted into a 96-well plate, followed by the addition of 200  $\mu$ L of BCA reagent (reagent A/reagent B = 50/1, v/v) to each well, and mixed thoroughly for 30 s. After 30 min incubation at 37  $^{\circ}$ C in the dark, the absorbance of the mixture was measured at 562 nm wavelength using a microplate reader. The protein concentration was calculated using the standard curve method.<sup>17</sup>

**TEM Imaging of Exosomes.** Five  $\mu$ L of exosome solution in DI water was placed onto a carbon-coated copper TEM grid and air-dried at room temperature for 15 min. For negative staining, 5  $\mu$ L of phosphotungstic acid (1%) was added to the grid, and the samples were examined using the TEM system. The average exosome size was determined by dynamic light scattering using the Zetasizer Nano after passing the exosome solution in PBS through a 0.45  $\mu$ m filter two times.<sup>26,41</sup>

**Western Blotting.** The exosomes were lysed in RIPA buffer containing protease inhibitors (1 $\times$ ). The exosomal lysate was denatured at 95  $^{\circ}$ C for 5 min, and equal amounts of protein (20  $\mu$ g) were resolved on 10% SDS-polyacrylamide gels, followed by the transfer to a polyvinylidene difluoride membrane at 100 V, 0.1 A, for 1 h 20 min at 4  $^{\circ}$ C. Next, the blots were blocked with 3% skim milk in TBS with Tween 20 (TBS-T: 10 mM Tris, pH 8.0, 150 mM, and NaCl solution containing 0.05% Tween 20) for 1 h at room temperature. The blots were washed 3 $\times$  with TBS-T (10 min each) and then incubated with primary antibodies diluted in skim milk (3%) solution as follows: anti-CD-63 (ab217345; Abcam), anti-Alix (ab186429; Abcam), and anti-Flotillin 1 (ab41927; Abcam) at 1:1000 dilution overnight at 4  $^{\circ}$ C. Next, the membranes were rinsed 3 $\times$  with TBS-T, incubated with goat anti-rabbit IgG H&L (HRP) (ab205718; Abcam, 1:2,000 dilution) for 1 h at room temperature, followed by signal development for 5 min. The blots were visualized using an enhanced chemiluminescence mode detection system.<sup>61</sup>

**Cellular Uptake of the Exosomes to 4T1 Cancer Cells.** One  $\times 10^6$  4T1 cells were plated on 12-well plate overnight for cell attachment. After that, the cells were incubated with DOX-TSLPs, microrobot-exos, or microrobot-exo + magnet at DOX concentration of 10  $\mu$ g/mL for 12 h. After that, the cells were harvested and examined under FACS system.

**TUNEL Assay.** Tumor tissues were harvested, processed, and mounted on the adhesive glass slides as mentioned above. The

staining procedure was followed by standard protocol using *in situ* Apoptosis Detection Kit (ab206386, Abcam). Briefly, each slide was covered with 100  $\mu\text{L}$  Proteinase K solution for 20 min. After rinsing with TBS for 5 min, 100  $\mu\text{L}$  of  $\text{H}_2\text{O}_2$  was applied to the slide, followed by 100  $\mu\text{L}$  TdT of equilibration buffer and incubated for 30 min. Next, 40  $\mu\text{L}$  of TdT labeling reaction mix was added to each sample, covered with a coverslip, and incubated at 37  $^\circ\text{C}$  for 90 min. The stop buffer (100  $\mu\text{L}$ ) was added to each slide and incubated for 5 min. Next, the blocking buffer (100  $\mu\text{L}$ ) was added, and the slides were incubated for 10 min. After carefully blotting the blocking buffer, 100  $\mu\text{L}$  of 1 $\times$  conjugate was applied immediately to each specimen and incubated for 30 min. The samples were then rinsed with TBS, covered with 100  $\mu\text{L}$  of DAB solution, and incubated for 15 min. The slides were washed once with DI water and counter-stained with 100  $\mu\text{L}$  of methyl green for 3 min. Finally, the slides were dehydrated in absolute ethanol, followed by xylene, and mounted using mounting media (ProLong Diamond Antifade Mountant, P36961, Thermo Fisher Scientific).

**Prussian Blue Staining.** Tumor tissues were harvested, processed, and mounted on the adhesive glass slides as mentioned previously. After the slides were washed with PBS, 1 mL of 4% potassium ferrocyanide (II) trihydrate and 4% HCl solution were added to each slide, and the slides were incubated for 10 min, with two changes. Next, the slides were briefly washed with PBS and counterstained with 1 mL of nuclear fast red solution for 3 min. After that, the slides were dipped into xylene and subsequently mounted using the xylene-based mounting medium. Finally, the tissues were observed under a fluorescent microscope (Ti-U, Nikon, Tokyo, Japan).

**Statistical Analysis.** All data are presented as mean  $\pm$  standard deviation (SD) of three or more samples. One-way analysis of variance followed by Tukey's multiple comparison test to determine statistical significance between the groups was performed using GraphPad Prism software (GraphPad Software, Inc.; San Diego, CA, USA). In addition, pairwise comparisons were also performed using the Student's *t*-test. *P*-values  $<0.05$  were considered statistically significant.

## ASSOCIATED CONTENT

### Supporting Information

The Supporting Information is available free of charge at <https://pubs.acs.org/doi/10.1021/acsnano.1c00114>.

Characterization of CA-MNPs; characterization of DOX-TSLPs; Bio-TEM images of slices of microrobots; FACS data of the cellular uptake of 4T1 cancer cells; evaluation of penetration into 4T1 tumor spheroids at different cut planes; quantitative analysis of penetration into 4T1 tumor spheroids; *in vivo* blood clearance rate of microrobots; blood biochemistry parameters of mice intravenously injected with different samples; H&E staining of mouse organs from different treatment groups; images of mice from different treatment groups at day 14 postinjection; survival data of balb/c mice treated with different samples (PDF)

## AUTHOR INFORMATION

### Corresponding Authors

**Jong-Oh Park** – School of Mechanical Engineering, Chonnam National University, Gwangju 61186, Korea; Korea Institute of Medical Microrobotics, Gwangju 61011, Korea; Email: [jop@kimiro.re.kr](mailto:jop@kimiro.re.kr)

**Eunpyo Choi** – School of Mechanical Engineering, Chonnam National University, Gwangju 61186, Korea; Korea Institute of Medical Microrobotics, Gwangju 61011, Korea; [orcid.org/0000-0002-9689-6520](https://orcid.org/0000-0002-9689-6520); Email: [eunpyochoi@jnu.ac.kr](mailto:eunpyochoi@jnu.ac.kr)

## Authors

**Van Du Nguyen** – School of Mechanical Engineering, Chonnam National University, Gwangju 61186, Korea; Korea Institute of Medical Microrobotics, Gwangju 61011, Korea; [orcid.org/0000-0001-5139-8491](https://orcid.org/0000-0001-5139-8491)

**Hyun-Ki Min** – Korea Institute of Medical Microrobotics, Gwangju 61011, Korea

**Ho Yong Kim** – Korea Institute of Medical Microrobotics, Gwangju 61011, Korea

**Jiwon Han** – Korea Institute of Medical Microrobotics, Gwangju 61011, Korea

**You Hee Choi** – Korea Institute of Medical Microrobotics, Gwangju 61011, Korea

**Chang-Sei Kim** – School of Mechanical Engineering, Chonnam National University, Gwangju 61186, Korea; Korea Institute of Medical Microrobotics, Gwangju 61011, Korea

Complete contact information is available at:

<https://pubs.acs.org/doi/10.1021/acsnano.1c00114>

## Notes

The authors declare no competing financial interest.

## ACKNOWLEDGMENTS

The authors would like to thank the Medical Microrobot Center at Chonnam National University for providing facilities. This research was supported by a grant from the Korea Health Technology R&D Project through the Korea Health Industry Development Institute (KHIDI), funded by the Ministry of Health & Welfare, the Republic of Korea (grant number: HI19C0642).

## REFERENCES

- (1) Felfoul, O.; Mohammadi, M.; Taherkhani, S.; de Lanauze, D.; Zhong Xu, Y.; Loghin, D.; Essa, S.; Jancik, S.; Houle, D.; Lafleur, M.; Gaboury, L.; Tabrizian, M.; Kaou, N.; Atkin, M.; Vuong, T.; Batist, G.; Beauchemin, N.; Radzioch, D.; Martel, S. Magneto-Aerotactic Bacteria Deliver Drug-Containing Nanoliposomes to Tumour Hypoxic Regions. *Nat. Nanotechnol.* **2016**, *11*, 941–947.
- (2) Alapan, Y.; Yasa, O.; Schauer, O.; Giltinan, J.; Tabak, A. F.; Sourjik, V.; Sitti, M. Soft Erythrocyte-Based Bacterial Microswimmers for Cargo Delivery. *Science Robotics* **2018**, *3*, No. eaar4423.
- (3) Deng, G.; Peng, X.; Sun, Z.; Zheng, W.; Yu, J.; Du, L.; Chen, H.; Gong, P.; Zhang, P.; Cai, L.; Tang, B. Z. Natural-Killer-Cell-Inspired Nanorobots with Aggregation-Induced Emission Characteristics for Near-Infrared-II Fluorescence-Guided Glioma Theranostics. *ACS Nano* **2020**, *14*, 11452–11462.
- (4) Xie, S.; Xia, T.; Li, S.; Mo, C.; Chen, M.; Li, X. Bacteria-Propelled Microrockets to Promote the Tumor Accumulation and Intracellular Drug Uptake. *Chem. Eng. J.* **2020**, *392*, 123786.
- (5) Zheng, D.-W.; Chen, Y.; Li, Z.-H.; Xu, L.; Li, C.-X.; Li, B.; Fan, J.-X.; Cheng, S.-X.; Zhang, X.-Z. Optically-Controlled Bacterial Metabolite for Cancer Therapy. *Nat. Commun.* **2018**, *9*, 1680.
- (6) Chen, W.; Wang, Y.; Qin, M.; Zhang, X.; Zhang, Z.; Sun, X.; Gu, Z. Bacteria-Driven Hypoxia Targeting for Combined Biotherapy and Photothermal Therapy. *ACS Nano* **2018**, *12*, 5995–6005.
- (7) Luo, C.-H.; Huang, C.-T.; Su, C.-H.; Yeh, C.-S. Bacteria-Mediated Hypoxia-Specific Delivery of Nanoparticles for Tumors Imaging and Therapy. *Nano Lett.* **2016**, *16*, 3493–3499.
- (8) Nguyen, V. D.; Han, J.; Go, G.; Zhen, J.; Zheng, S.; Le, V. H.; Park, J.-O.; Park, S. Feasibility Study of Dual-Targeting Paclitaxel-Loaded Magnetic Liposomes Using Electromagnetic Actuation and Macrophages. *Sens. Actuators, B* **2017**, *240*, 1226–1236.
- (9) Li, D.; Choi, H.; Cho, S.; Jeong, S.; Jin, Z.; Lee, C.; Ko, S. Y.; Park, J.-O.; Park, S. A Hybrid Actuated Microrobot Using an

Electromagnetic Field and Flagellated Bacteria for Tumor-Targeting Therapy. *Biotechnol. Bioeng.* **2015**, *112*, 1623–1631.

(10) Sun, P.; Deng, Q.; Kang, L.; Sun, Y.; Ren, J.; Qu, X. A Smart Nanoparticle-Laden and Remote-Controlled Self-Destructive Macrophage for Enhanced Chemo/Chemodynamic Synergistic Therapy. *ACS Nano* **2020**, *14*, 13894–13904.

(11) Zhang, Y.; Wang, Q.; Ma, T.; Zhu, D.; Liu, T.; Lv, F. Tumor Targeted Combination Therapy Mediated by Functional Macrophages under Fluorescence Imaging Guidance. *J. Controlled Release* **2020**, *328*, 127–140.

(12) Hou, T.; Wang, T.; Mu, W.; Yang, R.; Liang, S.; Zhang, Z.; Fu, S.; Gao, T.; Liu, Y.; Zhang, N. Nanoparticle-Loaded Polarized-Macrophages for Enhanced Tumor Targeting and Cell-Chemotherapy. *Nano-Micro Lett.* **2021**, *13*, 6.

(13) Zhang, F.; Mundaca-Urbe, R.; Gong, H.; Esteban-Fernández de Ávila, B.; Beltrán-Gastélum, M.; Karshalev, E.; Nourhani, A.; Tong, Y.; Nguyen, B.; Gallot, M.; Zhang, Y.; Zhang, L.; Wang, J. A Macrophage–Magnesium Hybrid Biomotor: Fabrication and Characterization. *Adv. Mater.* **2019**, *31*, 1901828.

(14) Choi, M.-R.; Stanton-Maxey, K. J.; Stanley, J. K.; Levin, C. S.; Bardhan, R.; Akin, D.; Badve, S.; Sturgis, J.; Robinson, J. P.; Bashir, R.; Halas, N. J.; Clare, S. E. A Cellular Trojan Horse for Delivery of Therapeutic Nanoparticles into Tumors. *Nano Lett.* **2007**, *7*, 3759–3765.

(15) An, L.; Wang, Y.; Lin, J.; Tian, Q.; Xie, Y.; Hu, J.; Yang, S. Macrophages-Mediated Delivery of Small Gold Nanorods for Tumor Hypoxia Photoacoustic Imaging and Enhanced Photothermal Therapy. *ACS Appl. Mater. Interfaces* **2019**, *11*, 15251–15261.

(16) Nguyen, V. D.; Min, H.-K.; Kim, D.-H.; Kim, C.-S.; Han, J.; Park, J.-O.; Choi, E. Macrophage-Mediated Delivery of Multifunctional Nanotherapeutics for Synergistic Chemo–Photothermal Therapy of Solid Tumors. *ACS Appl. Mater. Interfaces* **2020**, *12*, 10130–10141.

(17) Zhang, W.; Wang, M.; Tang, W.; Wen, R.; Zhou, S.; Lee, C.; Wang, H.; Jiang, W.; Delahunty, I. M.; Zhen, Z.; Chen, H.; Chapman, M.; Wu, Z.; Howerth, E. W.; Cai, H.; Li, Z.; Xie, J. Nanoparticle-Laden Macrophages for Tumor-Tropic Drug Delivery. *Adv. Mater.* **2018**, *30*, 1805557.

(18) Huang, L.; Yan, W.; Cai, B.; Song, Y.; Lv, Q.; Wang, G.; Wang, L.; Wang, Z. Dual-Engineered, “Trojanized” Macrophages Biomodally Eradicate Tumors Through Biologically and Photothermally Deconstructing Cancer Cells in an On-Demand, NIR-Commanded, Self-Explosive Manner. *Biomaterials* **2020**, *250*, 120021.

(19) Han, J.; Zhen, J.; Nguyen, V. D.; Go, G.; Choi, Y.; Ko, S. Y.; Park, J.-O.; Park, S. Hybrid-Actuating Macrophage-Based Microrobots for Active Cancer Therapy. *Sci. Rep.* **2016**, *6*, 28717.

(20) Chu, M.; Shao, Y.; Peng, J.; Dai, X.; Li, H.; Wu, Q.; Shi, D. Near-Infrared Laser Light Mediated Cancer Therapy by Photothermal Effect of Fe<sub>3</sub>O<sub>4</sub> Magnetic Nanoparticles. *Biomaterials* **2013**, *34*, 4078–4088.

(21) Xu, C.; Feng, Q.; Yang, H.; Wang, G.; Huang, L.; Bai, Q.; Zhang, C.; Wang, Y.; Chen, Y.; Cheng, Q.; Chen, M.; Han, Y.; Yu, Z.; Lesniak, M. S.; Cheng, Y. A Light-Triggered Mesenchymal Stem Cell Delivery System for Photoacoustic Imaging and Chemo-Photothermal Therapy of Triple Negative Breast Cancer. *Adv. Sci.* **2018**, *5*, 1800382.

(22) Choi, J.; Kim, H. Y.; Ju, E. J.; Jung, J.; Park, J.; Chung, H. K.; Lee, J. S.; Lee, J. S.; Park, H. J.; Song, S. Y.; Jeong, S. Y.; Choi, E. K. Use of Macrophages to Deliver Therapeutic and Imaging Contrast Agents to Tumors. *Biomaterials* **2012**, *33*, 4195–203.

(23) Qu, H.; Caruntu, D.; Liu, H.; O'Connor, C. J. Water-Dispersible Iron Oxide Magnetic Nanoparticles with Versatile Surface Functionalities. *Langmuir* **2011**, *27*, 2271–2278.

(24) Li, Y.; Zhou, X.; Wang, D.; Yang, B.; Yang, P. Nanodiamond Mediated Delivery of Chemotherapeutic Drugs. *J. Mater. Chem.* **2011**, *21*, 16406–16412.

(25) Mathew, B.; Ravindran, S.; Liu, X.; Torres, L.; Chennakesavalu, M.; Huang, C.-C.; Feng, L.; Zelka, R.; Lopez, J.; Sharma, M.; Roth, S. Mesenchymal Stem Cell-Derived Extracellular Vesicles and Retinal Ischemia-Reperfusion. *Biomaterials* **2019**, *197*, 146–160.

(26) Qi, H.; Liu, C.; Long, L.; Ren, Y.; Zhang, S.; Chang, X.; Qian, X.; Jia, H.; Zhao, J.; Sun, J.; Hou, X.; Yuan, X.; Kang, C. Blood Exosomes Endowed with Magnetic and Targeting Properties for Cancer Therapy. *ACS Nano* **2016**, *10*, 3323–3333.

(27) Huang, H.; Dong, Y.; Zhang, Y.; Ru, D.; Wu, Z.; Zhang, J.; Shen, M.; Duan, Y.; Sun, Y. GSH-Sensitive Pt(IV) Prodrug-Loaded Phase-Transitional Nanoparticles with A Hybrid Lipid-Polymer Shell for Precise Theranostics against Ovarian Cancer. *Theranostics* **2019**, *9*, 1047–1065.

(28) Wilhelm, S.; Tavares, A. J.; Dai, Q.; Ohta, S.; Audet, J.; Dvorak, H. F.; Chan, W. C. W. Analysis of Nanoparticle Delivery to Tumours. *Nat. Rev. Mater.* **2016**, *1*, 16014.

(29) Parayath, N. N.; Parikh, A.; Amiji, M. M. Repolarization of Tumor-Associated Macrophages in a Genetically Engineered Non-small Cell Lung Cancer Model by Intraperitoneal Administration of Hyaluronic Acid-Based Nanoparticles Encapsulating MicroRNA-125b. *Nano Lett.* **2018**, *18*, 3571–3579.

(30) Shi, C.; Liu, T.; Guo, Z.; Zhuang, R.; Zhang, X.; Chen, X. Reprogramming Tumor-Associated Macrophages by Nanoparticle-Based Reactive Oxygen Species Photogeneration. *Nano Lett.* **2018**, *18*, 7330–7342.

(31) Leonard, F.; Curtis, L. T.; Yesantharao, P.; Tanei, T.; Alexander, J. F.; Wu, M.; Lowengrub, J.; Liu, X.; Ferrari, M.; Yokoi, K.; Frieboes, H. B.; Godin, B. Enhanced Performance of Macrophage-Encapsulated Nanoparticle Albumin-Bound-Paclitaxel in Hypo-perfused Cancer Lesions. *Nanoscale* **2016**, *8*, 12544–52.

(32) Li, K.; Lu, L.; Xue, C.; Liu, J.; He, Y.; Zhou, J.; Xia, Z.; Dai, L.; Luo, Z.; Mao, Y.; Cai, K. Polarization of Tumor-Associated Macrophage Phenotype via Porous Hollow Iron Nanoparticles for Tumor Immunotherapy *in Vivo*. *Nanoscale* **2020**, *12*, 130–144.

(33) Lang, T.; Dong, X.; Huang, Y.; Ran, W.; Yin, Q.; Zhang, P.; Zhang, Z.; Yu, H.; Li, Y. Ly6Chi Monocytes Delivering pH-Sensitive Micelle Loading Paclitaxel Improve Targeting Therapy of Metastatic Breast Cancer. *Adv. Funct. Mater.* **2017**, *27*, 1701093.

(34) Huang, W.-C.; Chiang, W.-H.; Cheng, Y.-H.; Lin, W.-C.; Yu, C.-F.; Yen, C.-Y.; Yeh, C.-K.; Chern, C.-S.; Chiang, C.-S.; Chiu, H.-C. Tumortropic Monocyte-Mediated Delivery of Echogenic Polymer Bubbles and Therapeutic Vesicles for Chemotherapy of Tumor Hypoxia. *Biomaterials* **2015**, *71*, 71–83.

(35) Evans, M. A.; Huang, P.-J.; Iwamoto, Y.; Ibsen, K. N.; Chan, E. M.; Hitomi, Y.; Ford, P. C.; Mitragotri, S. Macrophage-Mediated Delivery of Light Activated Nitric Oxide Prodrugs with Spatial, Temporal and Concentration Control. *Chem. Sci.* **2018**, *9*, 3729–3741.

(36) Zheng, H.; Li, J.; Luo, X.; Li, C.; Hu, L.; Qiu, Q.; Ding, J.; Song, Y.; Deng, Y. Murine RAW264.7 Cells as Cellular Drug Delivery Carriers for Tumor Therapy: A Good Idea? *Cancer Chemother. Pharmacol.* **2019**, *83*, 361–374.

(37) Li, Z.; Huang, H.; Tang, S.; Li, Y.; Yu, X.-F.; Wang, H.; Li, P.; Sun, Z.; Zhang, H.; Liu, C.; Chu, P. K. Small Gold Nanorods Laden Macrophages for Enhanced Tumor Coverage in Photothermal Therapy. *Biomaterials* **2016**, *74*, 144–154.

(38) Kang, H.; Jung, H. J.; Kim, S. K.; Wong, D. S. H.; Lin, S.; Li, G.; Dravid, V. P.; Bian, L. Magnetic Manipulation of Reversible Nanocaging Controls *in Vivo* Adhesion and Polarization of Macrophages. *ACS Nano* **2018**, *12*, 5978–5994.

(39) Wu, L.; Zhang, F.; Wei, Z.; Li, X.; Zhao, H.; Lv, H.; Ge, R.; Ma, H.; Zhang, H.; Yang, B.; Li, J.; Jiang, J. Magnetic Delivery of Fe<sub>3</sub>O<sub>4</sub>@Polydopamine Nanoparticle-Loaded Natural Killer Cells Suggest a Promising Anticancer Treatment. *Biomater. Sci.* **2018**, *6*, 2714–2725.

(40) Kang, H.; Kim, S.; Wong, D. S. H.; Jung, H. J.; Lin, S.; Zou, K.; Li, R.; Li, G.; Dravid, V. P.; Bian, L. Remote Manipulation of Ligand Nano-Oscillations Regulates Adhesion and Polarization of Macrophages *in Vivo*. *Nano Lett.* **2017**, *17*, 6415–6427.

(41) Zhang, W.; Yu, Z.-L.; Wu, M.; Ren, J.-G.; Xia, H.-F.; Sa, G.-L.; Zhu, J.-Y.; Pang, D.-W.; Zhao, Y.-F.; Chen, G. Magnetic and Folate Functionalization Enables Rapid Isolation and Enhanced Tumor-Targeting of Cell-Derived Microvesicles. *ACS Nano* **2017**, *11*, 277–290.

- (42) Kim, H. Y.; Kim, T. J.; Kang, L.; Kim, Y.-J.; Kang, M. K.; Kim, J.; Ryu, J. H.; Hyeon, T.; Yoon, B.-W.; Ko, S.-B.; Kim, B.-S. Mesenchymal Stem Cell-Derived Magnetic Extracellular Nanovesicles for Targeting and Treatment of Ischemic Stroke. *Biomaterials* **2020**, *243*, 119942.
- (43) Kim, H. Y.; Kumar, H.; Jo, M. J.; Kim, J.; Yoon, J. K.; Lee, J. R.; Kang, M.; Choo, Y. W.; Song, S. Y.; Kwon, S. P.; Hyeon, T.; Han, I. B.; Kim, B. S. Therapeutic Efficacy-Potiated and Diseased Organ-Targeting Nanovesicles Derived from Mesenchymal Stem Cells for Spinal Cord Injury Treatment. *Nano Lett.* **2018**, *18*, 4965–4975.
- (44) Wang, C.; Xu, H.; Liang, C.; Liu, Y.; Li, Z.; Yang, G.; Cheng, L.; Li, Y.; Liu, Z. Iron Oxide @ Polypyrrole Nanoparticles as a Multifunctional Drug Carrier for Remotely Controlled Cancer Therapy with Synergistic Antitumor Effect. *ACS Nano* **2013**, *7*, 6782–6795.
- (45) Pang, L.; Qin, J.; Han, L.; Zhao, W.; Liang, J.; Xie, Z.; Yang, P.; Wang, J. Exploiting Macrophages as Targeted Carrier to Guide Nanoparticles into Glioma. *Oncotarget* **2016**, *7*, 37081–37091.
- (46) Nam, J.; Son, S.; Ochyl, L. J.; Kuai, R.; Schwendeman, A.; Moon, J. J. Chemo-Photothermal Therapy Combination Elicits Anti-Tumor Immunity against Advanced Metastatic Cancer. *Nat. Commun.* **2018**, *9*, 1074.
- (47) Jin, Z.; Nguyen, K. T.; Go, G.; Kang, B.; Min, H.-K.; Kim, S.-J.; Kim, Y.; Li, H.; Kim, C.-S.; Lee, S.; Park, S.; Kim, K.-P.; Huh, K. M.; Song, J.; Park, J.-O.; Choi, E. Multifunctional Nanorobot System for Active Therapeutic Delivery and Synergistic Chemo-Photothermal Therapy. *Nano Lett.* **2019**, *19*, 8550–8564.
- (48) Racuciu, M.; Creanga, D. E.; Airinei, A. Citric-Acid-Coated Magnetite Nanoparticles for Biological Applications. *Eur. Phys. J. E: Soft Matter Biol. Phys.* **2006**, *21*, 117–21.
- (49) Park, J.-H.; Cho, H.-J.; Yoon, H. Y.; Yoon, I.-S.; Ko, S.-H.; Shim, J.-S.; Cho, J.-H.; Park, J. H.; Kim, K.; Kwon, I. C.; Kim, D.-D. Hyaluronic Acid Derivative-Coated Nanohybrid Liposomes for Cancer Imaging and Drug Delivery. *J. Controlled Release* **2014**, *174*, 98–108.
- (50) Wang, C.; Yu, X.; Cao, Q.; Wang, Y.; Zheng, G.; Tan, T. K.; Zhao, H.; Zhao, Y.; Wang, Y.; Harris, D. C. Characterization of Murine Macrophages from Bone Marrow, Spleen and Peritoneum. *BMC Immunol.* **2013**, *14*, 6.
- (51) Agarwal, A.; Mackey, M. A.; El-Sayed, M. A.; Bellamkonda, R. V. Remote Triggered Release of Doxorubicin in Tumors by Synergistic Application of Thermosensitive Liposomes and Gold Nanorods. *ACS Nano* **2011**, *5*, 4919–4926.
- (52) Huang, W.-C.; Lu, I. L.; Chiang, W.-H.; Lin, Y.-W.; Tsai, Y.-C.; Chen, H.-H.; Chang, C.-W.; Chiang, C.-S.; Chiu, H.-C. Tumortropic Adipose-Derived Stem Cells Carrying Smart Nanotherapeutics for Targeted Delivery and Dual-Modality Therapy of Orthotopic Glioblastoma. *J. Controlled Release* **2017**, *254*, 119–130.
- (53) Nguyen, V. D.; Min, H.-K.; Kim, C.-S.; Han, J.; Park, J.-O.; Choi, E. Folate Receptor-Targeted Liposomal Nanocomplex for Effective Synergistic Photothermal-Chemotherapy of Breast Cancer *In Vivo*. *Colloids Surf., B* **2019**, *173*, 539–548.
- (54) Pang, L.; Zhu, Y.; Qin, J.; Zhao, W.; Wang, J. Primary M1 Macrophages as Multifunctional Carrier Combined with PLGA Nanoparticle Delivering Anticancer Drug for Efficient Glioma Therapy. *Drug Delivery* **2018**, *25*, 1922–1931.
- (55) Oh, N.; Kim, Y.; Kweon, H.-S.; Oh, W.-Y.; Park, J.-H. Macrophage-Mediated Exocytosis of Elongated Nanoparticles Improves Hepatic Excretion and Cancer Phototherapy. *ACS Appl. Mater. Interfaces* **2018**, *10*, 28450–28457.
- (56) Shao, D.; Zhang, F.; Chen, F.; Zheng, X.; Hu, H.; Yang, C.; Tu, Z.; Wang, Z.; Chang, Z.; Lu, J.; Li, T.; Zhang, Y.; Chen, L.; Leong, K. W.; Dong, W.-f. Biomimetic Diselenide-Bridged Mesoporous Organosilica Nanoparticles as an X-Ray-Responsive Biodegradable Carrier for Chemo-Immunotherapy. *Adv. Mater.* **2020**, *32*, 2004385.
- (57) Yu, G.-T.; Rao, L.; Wu, H.; Yang, L.-L.; Bu, L.-L.; Deng, W.-W.; Wu, L.; Nan, X.; Zhang, W.-F.; Zhao, X.-Z.; Liu, W.; Sun, Z.-J. Myeloid-Derived Suppressor Cell Membrane-Coated Magnetic Nanoparticles for Cancer Theranostics by Inducing Macrophage Polarization and Synergizing Immunogenic Cell Death. *Adv. Funct. Mater.* **2018**, *28*, 1801389.
- (58) Chen, Q.; Hu, Q.; Dukhovlina, E.; Chen, G.; Ahn, S.; Wang, C.; Ogunnaike, E. A.; Ligler, F. S.; Dotti, G.; Gu, Z. Photothermal Therapy Promotes Tumor Infiltration and Antitumor Activity of CAR T Cells. *Adv. Mater.* **2019**, *31*, 1900192.
- (59) Rao, L.; Bu, L.-L.; Meng, Q.-F.; Cai, B.; Deng, W.-W.; Li, A.; Li, K.; Guo, S.-S.; Zhang, W.-F.; Liu, W.; Sun, Z.-J.; Zhao, X.-Z. Antitumor Platelet-Mimicking Magnetic Nanoparticles. *Adv. Funct. Mater.* **2017**, *27*, 1604774.
- (60) Yong, T.; Zhang, X.; Bie, N.; Zhang, H.; Zhang, X.; Li, F.; Hakeem, A.; Hu, J.; Gan, L.; Santos, H. A.; Yang, X. Tumor Exosome-Based Nanoparticles Are Efficient Drug Carriers for Chemotherapy. *Nat. Commun.* **2019**, *10*, 3838.
- (61) Son, D. J.; Jung, Y. Y.; Park, M. H.; Lee, H. L.; Song, M. J.; Yoo, H.-S.; Hwang, D. Y.; Han, S. B.; Hong, J. T. Activated Natural Killer Cells Mediate the Suppressive Effect of Interleukin-4 on Tumor Development via STAT6 Activation in an Atopic Condition Melanoma Model. *Neoplasia* **2017**, *19*, 537–548.